

# Immune-Epithelial Dynamics and Tissue Remodeling in Chronically Inflamed Nasal Epithelium via Multi-scaled Transcriptomics

Guanrui Liao<sup>1,2,\*</sup>, Tsuguhsia Nakayama<sup>3,4,\*</sup>, Ivan T. Lee<sup>3,5,6,\*</sup>, Bokai Zhu<sup>6,\*</sup>, Dawn. T. Bravo<sup>3</sup>, Jonathan B. Overdevest<sup>7</sup>, Carol H. Yan<sup>8</sup>, David Zarabanda<sup>3</sup>, Philip A. Gall<sup>3</sup>, Sachi S. Dholakia<sup>3</sup>, Nicole A. Borchard<sup>3</sup>, Angela Yang<sup>3</sup>, Dayoung Kim<sup>3</sup>, Zara M. Patel<sup>3</sup>, Peter H. Hwang<sup>3</sup>, Dhananjay Wagh<sup>9</sup>, John Coller<sup>9</sup>, Katie Phillips<sup>10</sup>, Michael T. Chang<sup>3</sup>, Matt Lechner<sup>11</sup>, Qin Ma<sup>12,13</sup>, Zihai Li<sup>13</sup>, Garry Nolan<sup>6</sup>, Dan H. Barouch<sup>1</sup>, Jayakar V. Nayak<sup>3,14,✉</sup>, and Sizun Jiang<sup>1,15,16,✉</sup>

<sup>1</sup> Center for Virology and Vaccine Research, Beth Israel Deaconess Medical Center, Boston, MA, USA

<sup>2</sup> Center of Hepato-Pancreato-Biliary Surgery, The First Affiliated Hospital of Sun Yat-sen University, Guangzhou, Guangdong, People's Republic of China

<sup>3</sup> Department of Otolaryngology-Head and Neck Surgery, Stanford University School of Medicine, Stanford, CA, USA

<sup>4</sup> Department of Otorhinolaryngology-Head and Neck Surgery, Dokkyo Medical University, Tochigi, Japan

<sup>5</sup> Division of Allergy and Immunology, Boston Children's Hospital, Harvard Medical School, Boston, MA, USA

<sup>6</sup> Department of Pathology, Stanford University School of Medicine, Stanford, CA, USA

<sup>7</sup> Department of Otolaryngology-Head and Neck Surgery, Columbia University School of Medicine, New York, NY, USA

<sup>8</sup> Division of Otolaryngology – Head and Neck Surgery, Department of Surgery, University of California San Diego School of Medicine, University of California, San Diego, La Jolla, CA, USA

<sup>9</sup> Department of Genetics, Stanford University School of Medicine, Stanford, CA, USA

<sup>10</sup> Department of Otolaryngology-Head and Neck Surgery, University of Cincinnati School of Medicine, Cincinnati, OH, USA

<sup>11</sup> UCL Head and Neck Academic Centre, Division of Surgery and Interventional Science, University College London, London, UK

<sup>12</sup> Department of Biomedical Informatics, The Ohio State University, Columbus, OH, USA

<sup>13</sup> Pelotonia Institute for Immuno-Oncology, The James Comprehensive Cancer Center, The Ohio State University, Columbus, OH, USA

<sup>14</sup> Department of Otolaryngology-Head and Neck Surgery, Veterans Affairs Palo Alto Health Care System, Palo Alto, CA, USA

<sup>15</sup> Department of Pathology, Dana Farber Cancer Institute, Boston, MA, USA

<sup>16</sup> The Broad Institute of Harvard and MIT, Cambridge, MA, USA

\*Those authors contributed equally to this paper

†Corresponding Authors

1 **Chronic rhinosinusitis (CRS) is a common inflammatory disease of the sinonasal cavity that affects millions of individuals worldwide. The complex pathophysiology of CRS remains poorly understood, with emerging evidence implicating the orchestration between diverse immune and epithelial cell types in disease progression. We applied single-cell RNA sequencing (scRNA-seq) and spatial transcriptomics to both dissociated and intact, freshly isolated sinonasal human tissues to investigate the cellular and molecular heterogeneity of CRS with and without nasal polyp formation compared to non-CRS control samples. Our findings reveal a mechanism for macrophage-eosinophil recruitment into the nasal mucosa, systematic dysregulation of CD4+ and CD8+ T cells, and enrichment of mast cell populations to the upper airway tissues with intricate interactions between mast cells and CD4 T cells. Additionally, we identify immune-epithelial interactions and dysregulation, particularly involving understudied basal progenitor cells and Tuft chemosensory cells. We further describe a distinct basal cell differential trajectory in CRS patients with nasal polyps (NP), and link it to NP formation through immune-epithelial remodeling. By harnessing stringent patient tissue selection and advanced technologies, our study unveils novel aspects of CRS pathophysiology, and sheds light onto both intricate immune and epithelial cell interactions within the disrupted CRS tissue microenvironment and promising targets for therapeutic intervention. These findings expand upon existing knowledge of nasal inflammation and provide a comprehensive resource towards understanding the cellular and molecular mechanisms underlying this uniquely complex disease entity, and beyond.**

## Introduction

Chronic rhinosinusitis (CRS) is a recondite and heterogeneous inflammatory disease of the nasal and sinonasal cavities. Epidemiologic studies estimate the global prevalence of CRS to be approximately 12% (1, 2) with patient-rated symptom severity akin to heart disease and chronic back pain (1). CRS can be classified into two major subtypes based on the presence or absence of nasal polyps: CRS with nasal polyps (CRSwNP) and CRS without nasal polyps (CRSsNP). Of the total CRS population, CRSsNP typically accounts for 75-80% of patients seen vs. 20-25% for CRSwNP (3), although this proportion varies regionally. However, CRSwNP in particular is associated with higher disease burden from obstructive, eosinophil-rich, nasal polyposis and sinonasal outflow tract inflammation and infection, leading to an increased likelihood of recalcitrant symptoms such as sinus headaches, olfactory loss, and recurrent sinusitis. The pathogenesis of CRSwNP involves both innate and acquired Th2-immunity mediated by the nasal epithelium/mucosa due to stimulation by extrinsic antigens, but the interaction between immune cells, epithelial cells, and key molecular determinants driving disease progression, remains elusive.

The dynamic crosstalk between immune-epithelial systems plays a critical role in the pathogenesis of many diseases, including CRS (4-6). In addition to its role as a physical barrier against environmental challenges from pathogens, airborne particulates and allergens, the nasal epithelium generates cell-derived cytokines and chemokines involved in mediating autocrine and paracrine signaling. These events lead to

62 recruitment of diverse myeloid and lymphoid immune cells, 117  
63 that in turn release molecular mediators that invigorate or 118  
64 blunt downstream epithelial and immune cell functions, thus 119  
65 orchestrating signature acute vs. chronic inflammation. This 120  
66 subtle interplay between epithelial and immune cells is often 121  
67 bidirectional within the native tissue microenvironment, and 122  
68 involves multiple participants. 123

69 T cells naturally play a crucial role in the adaptive im- 124  
70 mune response, and are central for regulation of the immune- 125  
71 epithelial interactions responsible for CRS pathogenesis. In 126  
72 particular, CD4+ T cells can differentiate into various sub- 127  
73 populations based on the cytokine environment encountered. 128  
74 CD4+ Th2 cells produce cytokines such as interleukin-4 (IL- 129  
75 4), IL-5, and IL-13, that recruit and activate eosinophils and 130  
76 mast cells which have been well-established to play signifi- 131  
77 cant roles in the pathophysiology of CRSwNP (7). CD8+ T 132  
78 cells eliminate infected or damaged cells, with their specific 133  
79 contributions to CRS less appreciated. 134  
80 135

80 Mast cells, another key player in the pathogenesis of CRS, 136  
81 are involved in innate immunity release of a range of inflam- 137  
82 matory mediators, including histamine, prostaglandins, and 138  
83 leukotrienes (8). Elevated mast cell number in CRSwNP has 139  
84 been reported, with their activation linked to the presence of 140  
85 cytokines and chemokines that promote eosinophilic inflam- 141  
86 mation (9).

87 Basal cell differentiation is an important factor in the patho- 142  
88 genesis of CRS. The sinonasal epithelium is comprised of 143  
89 several distinct cell types, including basal cells along the 144  
90 epithelial basement membrane, as well as differentiated ciliated 145  
91 cells, and goblet cells oriented towards the airway lumen. 146  
92 Basal cell hyperplasia, a rise in basal cell numbers through 147  
93 cell division, has been detected in patients with CRSwNP 148  
94 (10, 11), although the physiological relevance and conse- 149  
95 quence has been unclear. Basal cells differentiate into the 150  
96 other major ciliated and goblet/secretory epithelial cell types 151  
97 in response to environmental stressors (12, 13), but whether 152  
98 this process in fostering the development of CRS through 153  
99 priming of epithelial-immune exchange is entirely uncertain. 154  
100 We have previously described prominent type II responses in 155  
101 macrophages, and laid the groundwork to better assess dis- 156  
102 tinctive inflammatory and epithelial cells and their contribu- 157  
103 tions to type II inflammatory profiles in CRSwNP patients 158  
104 (14). 159  
160

105 A better understanding of these mechanisms *in situ* is crucial 161  
106 for the development of more targeted and effective treatments 162  
107 for this common, challenging and debilitating upper airway 163  
108 disease. To achieve this, we applied single-cell sequencing to 164  
109 uncover the phenotypic composition and functional aspects 165  
110 of a discovery CRS clinical cohort (Fig.1A), and orthogo- 166  
111 nally utilized spatial transcriptomics to interrogate a valida- 167  
112 tion CRS cohort (Fig.1A) to untangle the key players and 168  
113 epithelial-immune interactions within inflamed nasal tissues, 169  
114 including CRSwNP. We envision such a resource will also be 170  
115 broadly applicable to the multitude of other nasal inflamma- 170  
116 tory diseases. 171

## Results

**Single-Cell Transcriptomic Analysis of the CRS Microenvironment.** We utilized single-cell transcriptomics for an in-depth analysis of the CRS epithelial and immune landscape on an initial discovery cohort of rigorously-selected patients (n = 5 healthy controls, n = 5 CRSsNP, n = 6 CRSwNP for both the NP and adjacent non-polyp ethmoid sinus mucosa, see Methods) (Fig.1A and S1A). We first identified the major immune cell types within the upper airway microenvironment (Fig.1B), as B, T, and myeloid lineages. The origins of the 32,775 total cells were displayed in a UMAP plot, with tissue types and patient samples color-coded (Fig.S1B) as well as representative genes across the immune cell repertoire (Fig.S1C). We further resolved 11 cell types (21,833 cells in total) present within the upper airway human tissue samples across healthy and CRS samples, including secretory, ciliated, basal, goblet, tuft and other epithelial cell types (Fig.1C). The epithelial cell origins were presented in a separate UMAP plot, with tissue types and patient samples color-coded (Fig.S1D), and representative canonical marker genes across the epithelial cell repertoire depicted (Fig.S1E). Signature gene expression patterns were further discriminated across both immune and epithelial cell types (Fig.1D), to gain detailed insight into the complex cellular composition and states in CRS tissues.

**Macrophage Polarization in CRS Nasal Polyps.** Given the postulated role of myeloid cells in CRS (10, 14), we further stratified the myeloid cluster into subtypes, including macrophages, monocytes, and dendritic cells (DCs) (Fig.2A). These subtypes were well represented across the healthy and CRS samples (Fig.S2A). We quantified the percent composition of the three main subtypes of macrophages identified (CCL4L2, MRC1, VEGFA), and observed little change between numbers of the more M1-like macrophages state (Fig.2B, left panel), while macrophage subtypes polarized towards M2-like gene expression were consistently and significantly elevated in CRSwNP compared to healthy controls or CRSsNP (Fig.2B, middle and right panels). A similar analysis was performed for the other myeloid cells without any notable differences (Fig.S2B). These results suggested that macrophage cell states, and not merely quantities, are dysregulated in CRSwNP. We thus performed differential gene analysis to identify differentially expressed genes (DEGs) responsible for the cell state differences between the macrophages from CRSsNP and CRSwNP tissues (Fig.2C). Amongst them were genes associated with antigen presentation, complement pathway activation, and chemokines linked to immune cell recruitment and activation (Fig.2C and Fig.S2C). Scoring of immunosuppressive M2 activity through a pre-curated set of genes (15, 16) confirmed the increased frequency of M2-polarized in polyp tissue from single-cell RNA-seq (Fig.2D) and spatial (Fig.S2D), compared to non-polyp ethmoid tissue.

**Macrophage Recruitment of Eosinophils in CRS Through CCL13 and CCL18.** Given the known role of

Figure 1

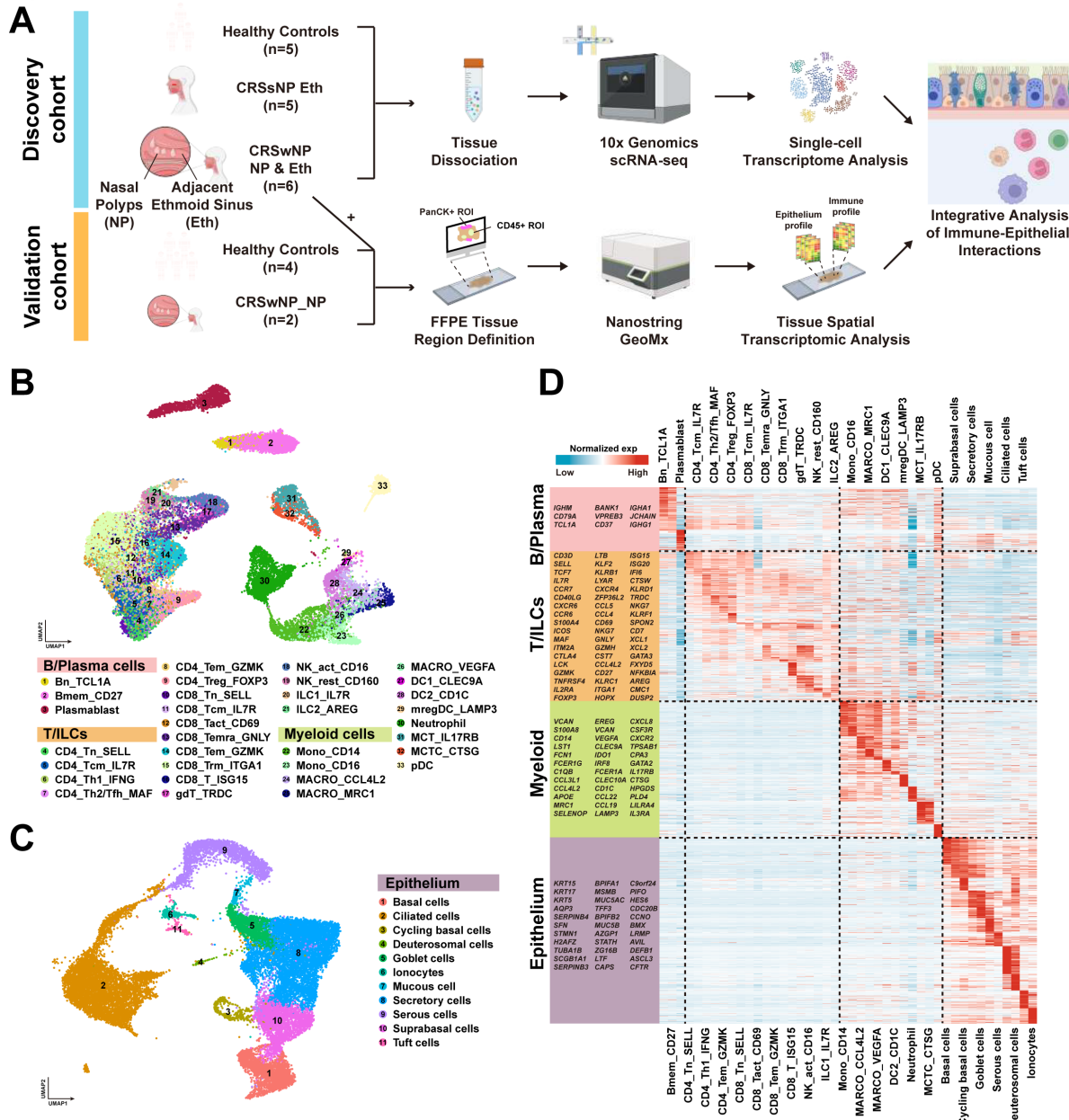


**Figure 1:** Comprehensive Single-Cell Transcriptomic Analysis Reveals the Complex Immune and Epithelial Microenvironment in CRS. (A) Schematic representation of the experimental workflow for the analyses conducted on CRS and control samples in the discovery and validation cohorts. CRSsNP - CRS without nasal polyp; CRSwNP - CRS with nasal polyps; (B) Uniform Manifold Approximation and Projection (UMAP) plot depicting 3 major cell types and 33 subtypes within the immune microenvironment of CRS, color-coded by cell type. (C) UMAP plot depicting the 11 epithelial cell types identified. (D) Heatmap depiction of the expression patterns of signature genes across the immune and epithelial cell types identified in panels (B) & (C), respectively.

172 CCL13 and CCL18 in CRSwNP (Fig.2A) for the recruitment of monocytes, including eosinophils (17, 18), we first 182 confirmed that eosinophils were increased in nasal polyp tissue 183 compared to control ethmoid tissues via spatial transcriptomics 184 (Fig.2E). This leverages upon the intact tissue microenvironment 185 preserved by spatial transcriptomics, since single-cell dissociation 186 approaches can often result in the loss of specific cell-types (19). We 187 next tested the hypothesis that CCL13 and CCL18 were involved in the 188 recruitment of eosinophils by macrophages (14). From our spatial 189 transcriptomics data, we observed significant correlations in the 190

scriptomics data, we observed significant correlations in the expression of both chemokines with heightened eosinophilic signatures in both the immune and epithelial tissue regions (Fig.2F). We next postulated that a location-based pairwise spatial analysis of these signatures would enable insights into the dynamics of eosinophil recruitment by macrophages. We observed a strong correlation between CCL13 and CCL18 expression with the influx of eosinophils in the pan-cytokeratin (PanCK)-positive epithelial, but not CD45-positive immune regions (Fig.2G and Fig.S2E). Similarly, the correlative ex-

Figure 2

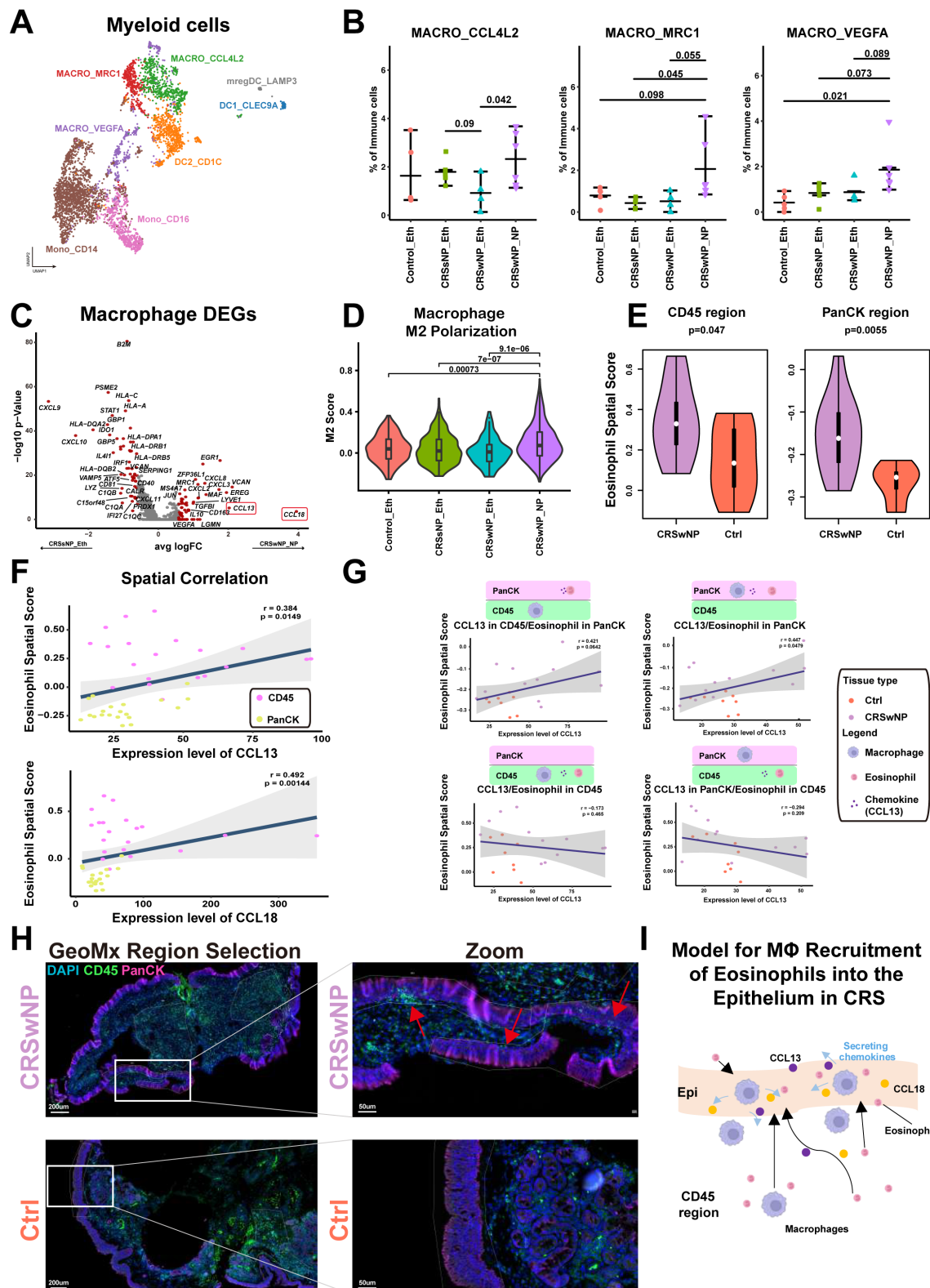


**Figure 2: Polarization of Macrophages to M2 Phenotype Drives Type 2 Inflammation in CRS Nasal Polyps.** (A) UMAP plot depicting subtypes and corresponding annotations of myeloid cells in CRS and healthy control samples. (B) Comparison of macrophage cell fractions between CRS and control samples using the Wilcoxon test (two-sided). (C) Volcano plot displaying differentially expressed genes in macrophages between CRSsNP and CRSwNP, with the most significant genes indicated in red ( $|Foldchange| > 1.5$ ), including CCL13 and CCL18. (D) Violin plots illustrating M2 scores for macrophages across CRS and control samples, with comparisons performed using the Wilcoxon test (two-sided) and p values indicated. (E) Violin plots comparing eosinophil spatial signature expression scores between CRS nasal polyps (purple) and healthy control samples (orange) in spatial transcriptomics GeoMx data within CD45+ regions (left panel) and PanCK+ regions (right panel), with comparisons performed using the Wilcoxon test (two-sided) and p values indicated.

**Figure 2 continue:** (F) Scatter plots demonstrating the correlation between *CCL13* (upper panel) or *CCL18* (lower panel) mRNA expression levels in situ, and eosinophil spatial signature expression scores in GeoMx data, with data origins colored to indicate CD45+ regions (magenta) and PanCK+ regions (yellow). The data was fitted using a linear regression model, with blue lines indicating the mean and grey regions highlighting the 95% confidence intervals. The regression index and p values are provided within the plots. (G) Scatter plots illustrating the correlation between *CCL13* expression levels and eosinophil signature scores in CD45+ or PanCK+ regions of GeoMx Spatial Transcriptomics acquisition, with sample origins color-coded to represent CRS nasal polyps (purple) and healthy control samples (orange). Diagrams above the scatter plots indicate regions where *CCL13* and eosinophil spatial gene signatures were captured. (H) Representative multiplexed immunofluorescence images from the GeoMx spatial transcriptome acquisition from a CRSwNP sample (upper panel) and a healthy control sample (lower panel). Red arrows highlight immune infiltration into the epithelial region, as indicated by CD45-positive cells within the PanCK region. White outlines indicate the region from which the transcriptome was extracted for the GeoMx experiment. (I) The proposed model in which macrophages secreting *CCL13/CCL18* chemokines attract eosinophils to infiltrate the epithelium in CRS nasal polyps.

192 expression of *CCL18* and its receptor, *CCR2*, also supported 240  
193 a case of directionality in the attraction of eosinophils into 241  
194 the epithelial region, but not the immune region, of the CRS 242  
195 nasal tissues. 242

196 Representative immunofluorescence images from the tissues 243  
197 stained for GeoMx, and regions defined for spatial tran- 244  
198 scriptomics data collection, further substantiated the local- 245  
199 ization of immune cell infiltration into the epithelial re- 246  
200 gions in CRSwNP, but not healthy control mucosal tissues 247  
201 (Fig.2H). Taken together, these results suggest a model, in 248  
202 which macrophages secreting *CCL13/CCL18* in CRSwNP 249  
203 are directing recruitment to, and subsequent trafficking of, 250  
204 eosinophils into the nasal epithelium in CRSwNP disease 251  
205 (Fig.2I) (14). 252

253 compared to CRSsNP (21).

## Mast Cell Enrichment and Type 2 Immune Responses in Nasal Polyps.

Given the intricate relationship between mast cells (MCs) and the type II immune response in T cells, we sought to better define the possible role of mast cells in CRSwNP disease (9). We observed two major subtypes of mast cells, stratified into 1) epithelial MCs expressing TPSAB1 tryptase without CMA1 chymase, with high expression of interleukin 17 Receptor B (termed MCT\_IL17RB), and 2) subepithelial MCs with high expression of the tryptase protease, along with Cathepsin G (CTSG) and chymase (termed MCTC\_CTSG) (Fig.4A). Both MC subtypes were found to be enriched in CRSwNP compared with other sample types (Fig.4B). The expression patterns of signature genes in these two mast cell subtypes were visibly distinct (Fig.4C), channeling the nuanced different cell states and functions within the CRSwNP tissue microenvironment. We therefore postulated that these mast cells subtypes may have distinct roles in the recruitment and interaction with key immune players within the CRSwNP tissue microenvironment. We tested this hypothesis via Ligand-Receptor (L-R) analysis and identified several pathways for immune and tissue remodeling related to CD4+ T cells, including *IL2*, *OX40*, *CCL*, *EPHB*, *PROS*, *IL4/IL13*, *PARs*, *CD22*, *ICAM*, *SEMA7*, *LIFR*, *CLEC*, and *OSM* (Fig.4D). Of particular interest were the key cytokine mediators in Type II inflammation: *IL4* and *IL13* (Fig.4D), which was predominantly expressed by MCs in our study (Fig.4E), and were implicated in MC and CD4+ T cell interactions in CRSwNP and not CRSsNP (Fig.4F). The CSF2 signaling pathway served as a control (Fig.4F). While similar trends were observed in each of the mast cell clusters (Fig.S4A-E), the MCT\_IL17RB mast cells exhibited a higher potential for immune interaction in CRSwNP as previously reported (22).

## Identification of Key Players in the Immune-Epithelial Crosstalk and Remodeling in CRSwNP.

Given the data from our work and others on the emerging evidence of immune-epithelial crosstalk and remodeling in multiple diseases (5, 6), including CRSwNP (4), we postulated that quantifying cell abundance correlations between immune and epithelial cell subsets in CRS and control samples would identify potential key players in this axis. Our analysis revealed a key cluster of epithelial and immune cell types that were strongly correlated with each other, indicative of their potential interplay in the epithelial-immune crosstalk and remodeling in CRSwNP (Fig.5A; black box). We specifically observed the enrichment of Tuft cells, cycling basal cells, and

206 **Immunosuppressive CD4+ and CD8+ T Cell Re- 254**  
207 **sponses Predominate in Nasal Polyps.** Detailed anal- 255  
208 ysis of CD4+ T cells and their subtypes revealed several 256  
209 categories represented across the control and CRS samples 257  
210 (Fig.3A and Fig.S3A). We identified an enrichment of CD4+ 258  
211 T effector memory (TEM), Th2, and T regulatory (Treg) 259  
212 CD4+ subtypes in CRSwNPs, and a depletion of Th1 CD4+ 260  
213 cells as previously described (Fig.3B and Fig.S3B) (20). 261  
214 Differential gene expression analysis and pathway enrich- 262  
215 ment analysis demonstrated significant differences between 263  
216 CD4+ T cells within the CRSsNP and CRSwNP microen- 264  
217 vironment (Fig.3C and Fig.3D), especially when compared 265  
218 against healthy controls (Fig.S3C). We confirmed the in- 266  
219 creased CD4+ T cell immunosuppression within CRSwNP 267  
220 compared to CRSsNP as demonstrated by Th2-skewed in- 268  
221 flammation from the scRNAseq cohort (Fig.3E), a reduction 269  
222 of immune cells related to the Th1 pathway, and an increase 270  
223 of immune cells towards the Th2 pathway from spatial tran- 271  
224 scriptomics (Fig.S3D). 272

225 Similarly, we investigated and identified lymphocyte sub- 273  
226 types and corresponding annotations in CD8+ T cells in both 274  
227 CRS and control samples (Fig.3F and Fig.S3E). Similar to 274  
228 our CD4+ T cell analysis, we also identified the enrich- 275  
229 ment of TEMs in the CRSwNP samples, along with a re- 276  
230 duction in CD8+ resident memory T cell phenotypes (Fig.3G 277  
231 and Fig.S3F). Differential gene expression analysis and path- 278  
232 way enrichment analysis also discriminated significant differ- 279  
233 ences in CD8+ T cells between the CRSsNP and CRSwNP 280  
234 microenvironment (Fig.3H and Fig.3I), along with altered 281  
235 inflammation (Fig.3J), in line with the CD4+ T cell find- 282  
236 ings (Fig.3E and Fig.S3D). These results support a model in 283  
237 which suppressor and regulatory T cells, including players in- 284  
238 volved in a type II immune response and Tregs, are responsi- 285  
239 ble for the unique chronic inflammatory features of CRSwNP 286

**Figure 3**

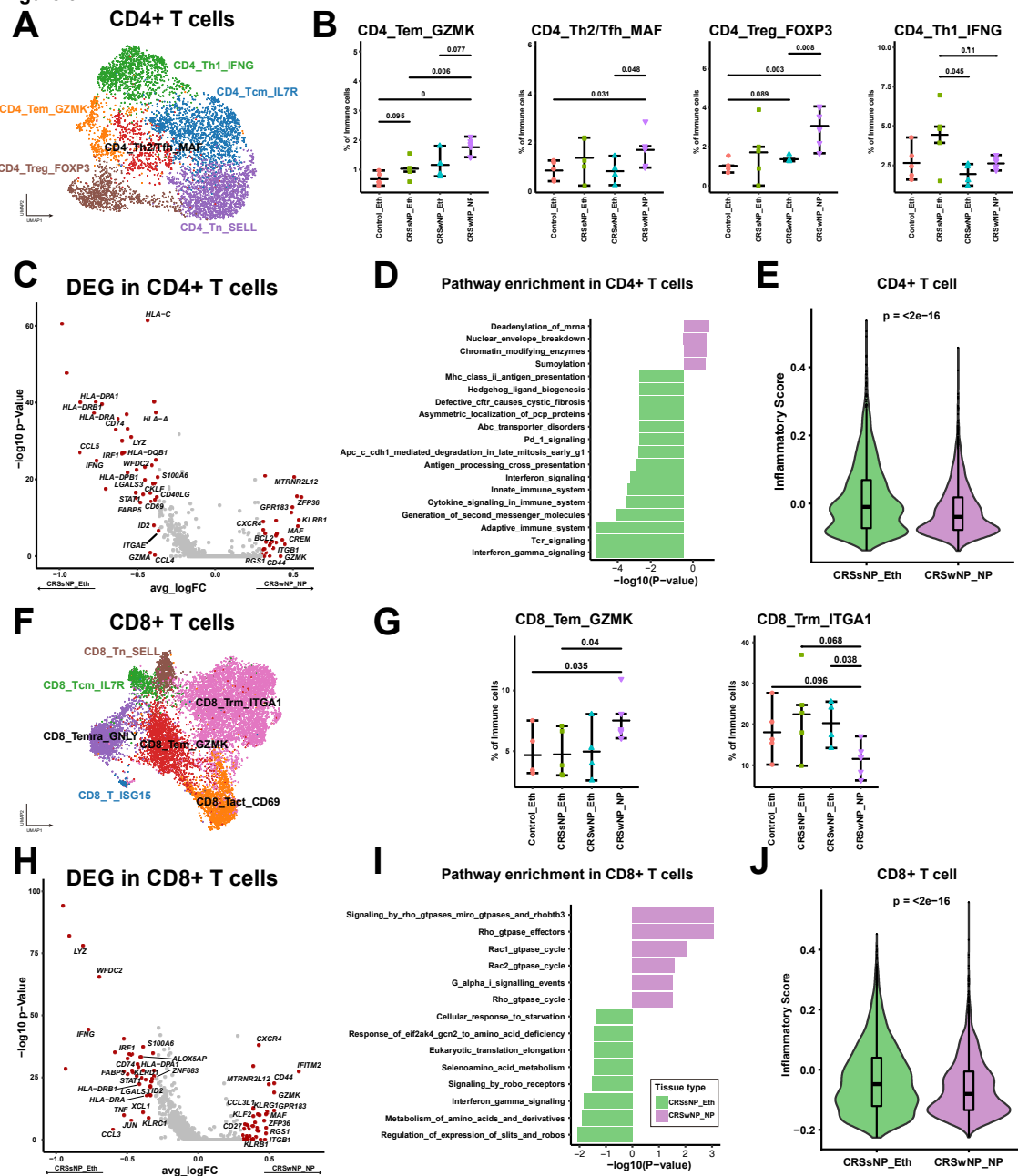


**Figure 3: Regulatory CD4+ and CD8+ T Cells Predominate in Nasal Polyps.** (A) UMAP plot illustrating subtypes and corresponding annotations of CD4+ T cells in CRS and control samples. (B) Comparison of CD4+ T cell fractions between CRS and control samples using the Wilcoxon test. (C) Volcano plot displaying differentially expressed genes in CD4+ T cells between CRSsNP and CRSwNP, with the most significant genes indicated in red ( $|Foldchange| > 1.25$ ). (D) Pathways enriched in CD4+ T cells from CRSsNP and CRSwNP, based on GSEA analysis using the REACTOME gene set. (E) Violin plots illustrating CD4+ T cell inflammatory signature expression scores in CRS and control samples, with comparisons performed using the Wilcoxon test (two-sided) and p values indicated. (F) UMAP plot depicting subtypes and corresponding annotations of CD8+ T cells in CRS and control samples. (G) Comparison of CD8+ T cell fractions between CRS and control samples using the Wilcoxon test (two-sided). (H) Volcano plot showing differentially expressed genes in CD8+ T cells between CRSsNP and CRSwNP, with the most significant genes indicated in red ( $|Foldchange| > 1.25$ ). (I) Pathways enriched in CD8+ T cells from CRS nasal polyps versus CRS without nasal polyps, based on GSEA analysis using the REACTOME gene set. (J) Violin plots presenting CD8+ T cell inflammatory signature expression scores in CRS and control samples, with comparisons performed using the Wilcoxon test (two-sided) and p values indicated.

Figure 4

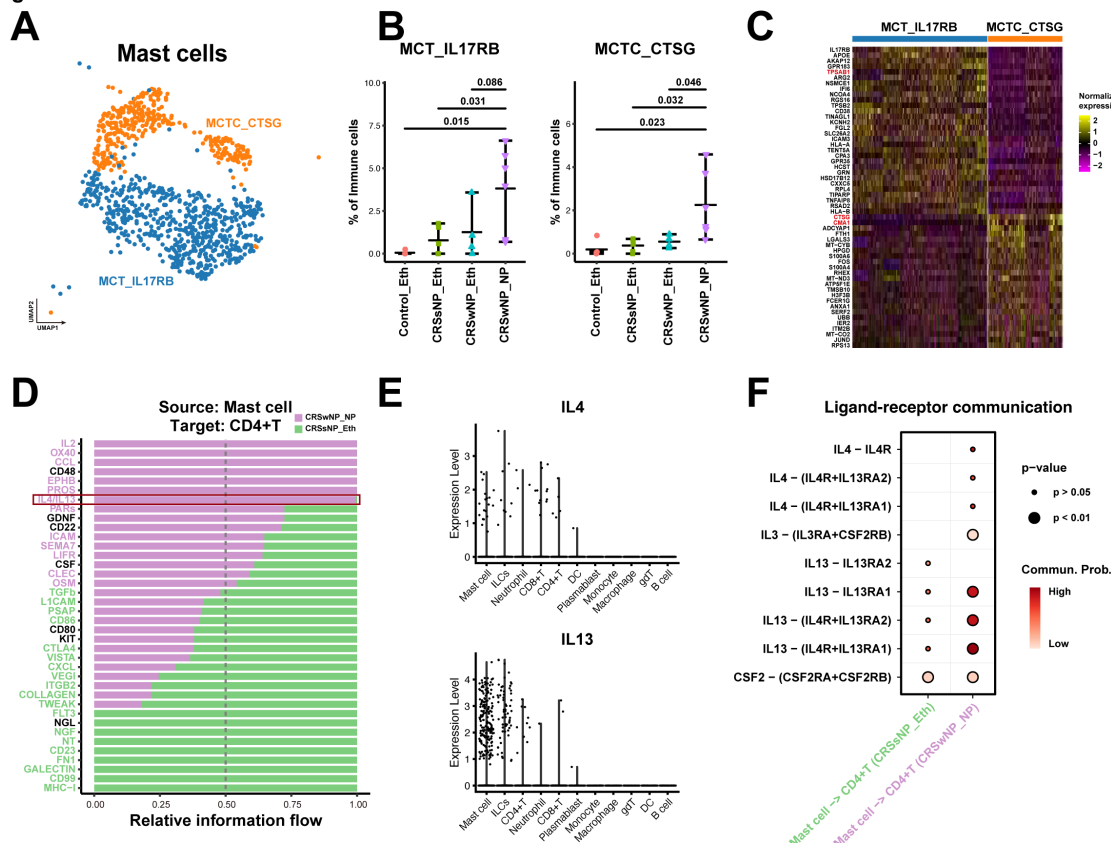


**Figure 4:** Mast Cell Enrichment in Nasal Polyps Correlates with Type 2 Immune Responses. (A) UMAP plot illustrating subtypes and corresponding annotations of mast cells in CRS and control samples. (B) Comparison of mast cell subtype fractions between CRS and control samples using the Wilcoxon test (two-sided). (C) Heatmap displaying normalized expression level of signature genes in the mast cell subtypes identified. (D) Ligand-receptor (L-R) interactions identified between mast cells and CD4+ T cells in CRSwNP (purple) and CRSSNP (green). L-R pairs with purple bars crossing the 0.5 dotted line indicate predominance in CRSwNP, while those with green bars crossing the dotted line indicate predominance in CRSSNP. Significant interactions are color-coded accordingly ( $p < 0.05$ , Wilcoxon test, two sided). (E) Scatter plots depicting IL4 and IL13 expression levels in various immune cells, and their dominant expression in Mast cells. (F) Dot plot demonstrating the significance and strength of IL4/IL13-related ligand-receptor interactions between mast cells and CD4+ T cells in CRSwNP (purple) and CRSSNP (green).

suprabasal cells as enriched in CRSwNP polyps, and the con- 308 versely depletion of FoxJ1 low ciliated cells, mucous cells 309 and serous cells in CRSwNP polyps (Fig.5B and Fig.S5). 310 These results warrant further investigation of Tuft cells and 311 basal cells as key players in mediating the immune-epithelial 312 crosstalk and attraction of immune infiltrates in the context 313 of chronic inflammation with nasal polyps formation. 314

We identified multiple cell-signaling pathways (including 315 G protein, Tyrosine Kinase, and MAP Kinase members), 316 anti-apoptotic genes (i.e. *BCL2*), and cytokine pathways (i.e. *IL17RB*, *IL13TA1*, *STAT6*) upregulated in CR- 317 SwNP (Fig.5C). Conversely, components of the antigen- 318 presentation pathway were upregulated in CRSSNP (Fig.5C), 319 implicating different cell states of the tuft cells in CRSwNP 320 as opposed to CRSSNP. We next identified additional path- 321 ways enriched in Tuft cells in CRSwNP, particularly the 322 prostaglandin pathway (Fig.5D), an inflammatory pathway 323 previously not described in the context of CRS. Gene Set En- 324 richment Analysis orthogonally confirmed the activation of 325 the prostaglandin pathway in CRSwNP (Fig.5E), along with 326 the expression of key members of this pathway, *ALOX5* and 327

PTGS1, in CRSwNP polyps and adjacent ethmoid tissues, 328 suggestive of high prostaglandin pathway activity in Tuft 329 cells within and outside of nasal polyps (Fig.5F). Ligand- 330 receptor analysis revealed significant pairing of tuft cell in- 331 teractions with Th2 CD4+ T cell recruitment in CRSwNP, 332 as well as depletion of naive and central memory CD4+ T 333 cells (Fig.5G), in line with our abundance correlative analy- 334 sis (Fig.5A). We next confirmed the increased density of tuft 335 cells within the CRSwNP epithelial layer in situ through spa- 336 tial transcriptomics (Fig.5H), to support the hypothesized tis- 337 sue interactions between Tuft cells in the PanCK+ region and 338 Th2 CD4+ T cells in CD45+ region of the CRSwNP tissue 339 (Fig.5I). These results strongly implicate chemosensory tuft 340 cells as one of the epithelial mediators of immune cell recruit- 341 ment, including recruiting CD4+ Th2 cells into the CRSwNP 342 inflammatory microenvironment to prime Type II inflamma- 343 tion.

**Identification of a Basal Cell Trajectory That Drives Key Epithelial-Immunologic Remodeling for Nasal Polyp Formation.** We finally investigated the role of basal

Figure 5

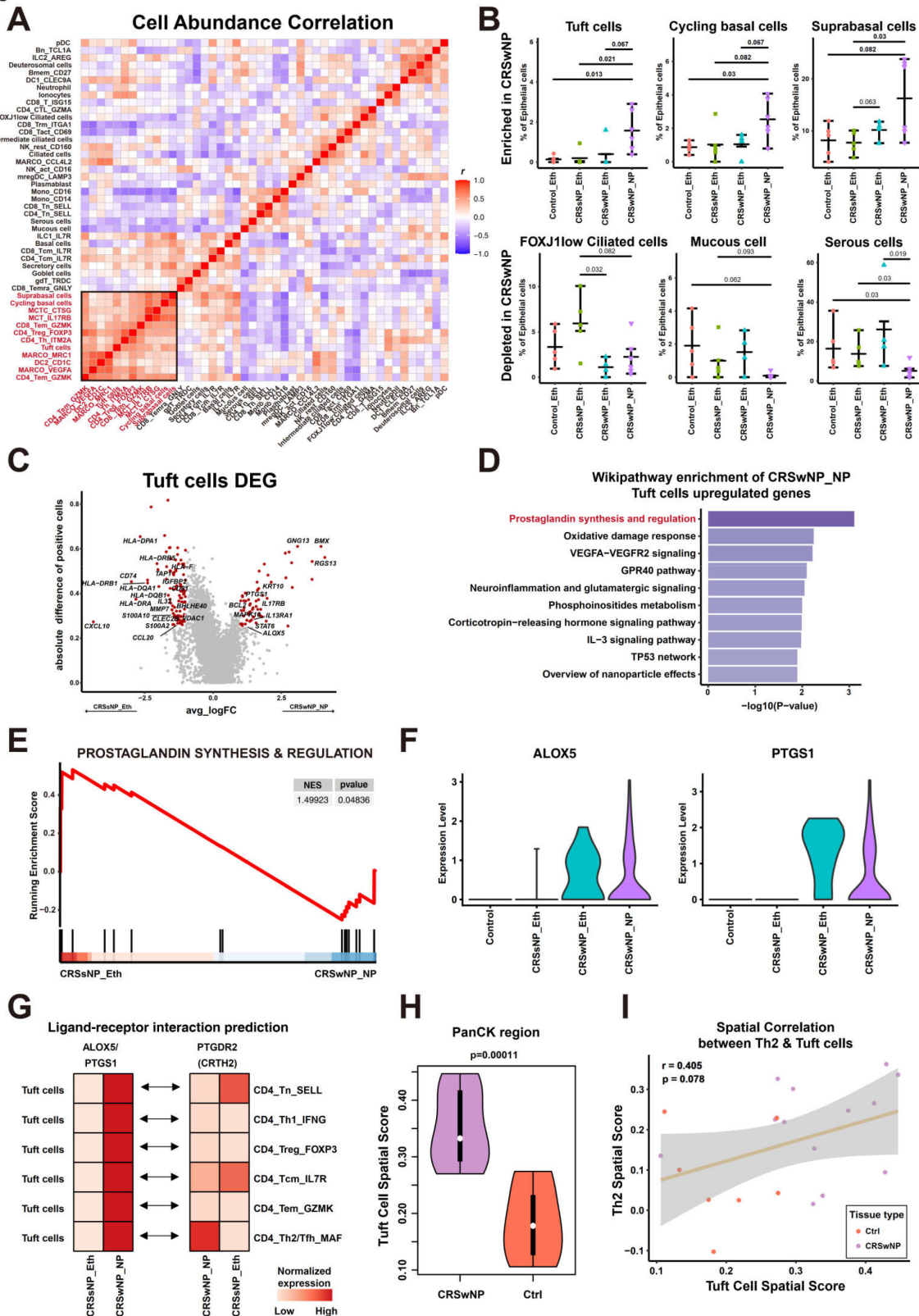


**Figure 5: Tuft Cells in Nasal Polyps Correlate with Th2 Cells.** (A) Heatmap illustrating cell abundance correlations between immune and epithelial cell fractions. (B) Comparison of epithelial cell subtype fractions between CRS and control samples using the Wilcoxon test (two-sided). (C) Volcano plot depicting differentially expressed genes in Tuft cells between CRSwNP and CRSsNP. The most significant genes are highlighted in red ( $|Foldchange| > 2$  and  $\Delta pct > 0.25$ ). (D) Pathways enriched in Tuft cells from CRSwNP versus CRSsNP, based on WIKIPATHWAY enrichment analysis. (E) Enrichment plot of the prostaglandin synthesis and regulation pathway in Tuft cells from CRSwNP versus CRSsNP, using GSEA analysis with the WIKIPATHWAY gene set. The enrichment score and p-value are indicated in the plot. (F) Violin plot displaying expression levels of ALOX5 and PTGS1 in CRS and control samples. (G) Ligand-receptor interaction prediction between ALOX5/PTGS1 and PTGDR2 (CRTH2) across Tuft cells, CRSsNP\_Eth, and CRSwNP\_NP. (H) PanCK region spatial scores for CRSwNP and Control (Ctrl) samples. (I) Scatter plot showing the spatial correlation between Th2 and Tuft cells. A linear regression line is shown with  $r = 0.405$  and  $p = 0.078$ .

**Figure 5 continue:** (G) Heatmap presenting mean expression levels of ALOX5/PTGS1 ligands in Tuft cells and mean expression levels of their PTGDR2 receptor in CD4+ T cell subsets in CRSwNP and CRSsNP. (H) Violin plots comparing Tuft cell spatial gene signature expression scores between CRSwNP (purple) and healthy controls (orange) in GeoMx spatial transcriptomics data within PanCK+ tissue regions. (I) Scatter plot and regression line illustrating the correlation between Tuft cell spatial gene signature expression scores in PanCK+ regions and Th2 cell spatial gene signature expression scores in CD45+ regions. Dots are colored to represent patient sample origins. The grey region indicates the confidence interval. The regression index and p-values are shown in the plots.

328 cells, which were also implicated as critical in CRSwNP 379 epithelial-immune remodeling (Fig.5A and 5B). We observed 380 differences in the expression of key genes between suprabasal 381 cells and cycling basal cells (Fig.6A and Fig.S6A), which 382 included a sizable overlap of key genes upregulated in CR- 383 SwNP compared to CRSsNP (Fig.S6B). Given the prolifer- 384 ative and developmental potential of basal cells, including 385 towards differentiated and/or specialized cell fates, we pos- 386 tulated that a cell trajectory analysis would allow us to track 387 differentiation states of the basal cells. Using the pseudotime 388 analysis, we confirmed that undifferentiated basal cells tend 389 to be present at a much earlier pseudotime point, followed by 390 a bifurcation in basal cell developmental trajectory, which 391 we termed Cell-fate1 and Cell-fate2 (Fig.6B). We observed 392 an enrichment of basal cells from CRSwNP patients in Cell- 393 fate2, while those from control and CRSsNP tissues were 394 associated with Cell-fate1 (Fig.6C-D), suggesting disparate 395 outcomes and cell states for the differentiated basal cells in 396 CRSwNP upper airway milieu compared to the CRSsNP mi- 397 croenvironment. 398 We stratified Cell-fate1 and Cell-fate2 to reveal important dif- 399 ferences in genes and pathways associated with each basal 400 cell fate (Fig.6E-F), including an enrichment of IL4 and 401 IL13 signaling, and cell-cell communication in CRSwNP 402 (Fig.6G), in contrast to heightened IFN signaling and anti- 403 gen presentation seen in CRSsNP (Fig.S6C). Cell-fate2 for 404 basal cells also correlated with multiple metabolic, immune 405 attractant, and tissue remodeling pathways (Fig.6E). A potent 406 link between Cell-fate2 basal cells and eosinophil infiltration 407 was further delineated by spatial transcriptomic analysis 408 (Fig.S6D). Spatial transcriptomic (Fig.6H) and reconstruc- 409 tion of the pseudotime trajectory also confirmed the enrich- 410 ment of Cell-fate2 basal cells in CRSwNP tissues (Fig.S6E- 411 F), and further highlighted the deviation towards key basal 412 Cell-fate2 pathways in CRSwNP (Fig.S6G-H). We observed 413 an increase in basal-immune cell interactions from scRNA- 414 seq in Cell-fate2 directed basal cells (Fig.6I), and increased 415 enrichment of pathways related to metabolism, IL4/IL13 416 signaling, neutrophil degranulation, and tissue remodeling 417 (Fig.6J). These results suggest that basal cells from CRSwNP 418 patients may differentiate towards a cellular state that is more 419 conducive for immune system co-mingling along with tissue 420 remodeling such as polyp formation, implicating basal cells 421 and this Cell-fate2 differentiation pathway as a pivotal deter- 422 minant for NP formation through epithelial-immune signal- 423 ing and remodeling.

374 **A Reduction in the Cell-Fate2 Basal Cell Trajectory** 424  
375 **Upon Use of Immunotherapeutics Intervention for CR-** 425  
376 **SwNP.** The upregulation of *IL4* and *IL13* in CRSwNP dis- 426 ease, and in basal Cell-fate2 trajectory, implicates the cen- 427 tral role of basal cells in coordinating CRSwNP and NP 428

development. This was further supported by results from IL4 and IL13 cytokine stimulation of non-NP derived basal cells (10), indicating a skew towards the Cell-fate2 signature (Fig.S6I). Dupilumab is an IL-4/-13 receptor alpha antagonist that is FDA-approved as a primary and/or maintenance treatment in adult patients with poorly controlled CRSwNP (23, 24). Inferior turbinate and NP tissues sampled pre- and post-dupilumab treatment were reanalyzed using scRNA-seq (10), and found to have a statistically significant reduction in Cell-fate2 transcriptomic signature in basal cells (Fig.6K). Taken together, these results clarify the role of basal cells and the Cell-fate2 developmental trajectory as the center of both epithelial-immune system interactions and remodeling in NP formation in patients suffering from chronic rhinosinusitis.

## Discussion

The present study provides an in-depth analysis of the complex immune and epithelial landscape in chronic rhinosinusitis (CRS) without and without nasal polyps, through single-cell transcriptomic profiling, and orthogonal interrogation of the intact tissue microenvironment with spatial transcriptomics. Our findings begin to unravel intricate immune-epithelial interactions and remodeling at play in nasal polyp tissues, thus shedding light on the cellular and molecular mechanisms that drive the pathogenesis of CRS, particularly related to NP formation.

In CRSwNP disease, our data outlined a role for macrophage polarization and recruitment of eosinophils into the epithelial compartment (Fig.2), Type II inflammatory activation in T cells (Fig.3), *IL4* and *IL13* activation in MCs and interactions with CD4+ T cells (Fig.4), an epithelial-immune axis harbored by Tuft cells (Fig.5) and basal cells (Fig.6), and a unique differential pathway for basal cells associated with NP formation (Fig.6). Notably, we observed polarization of macrophages towards an M2 phenotype specifically in CRSwNP that primes Type 2 inflammation. The M2 macrophages were found to secrete *CCL13* and *CCL18*, which are potent chemokines that promote eosinophilic infiltration into the upper airway epithelium. This observation emphasizes the role of macrophages in coordinating and molding the inflammatory milieu in inflammatory CRS nasal polyp disease, and their potential as a therapeutic target for modulating Type II inflammation.

These data also revealed the predominance of 'immunosuppressive' Type II-skewed CD4+ and CD8+ T cells within nasal polyps, further highlighting the crosstalk between macrophages and T cells in this common form of chronic sinonasal immunity. This interplay between immune cells within upper airway microenvironment suggests the presence of an intricate balance between pro-inflammatory and regulatory T cell subsets in distinct CRS fates, with potential impli-

**Figure 6**

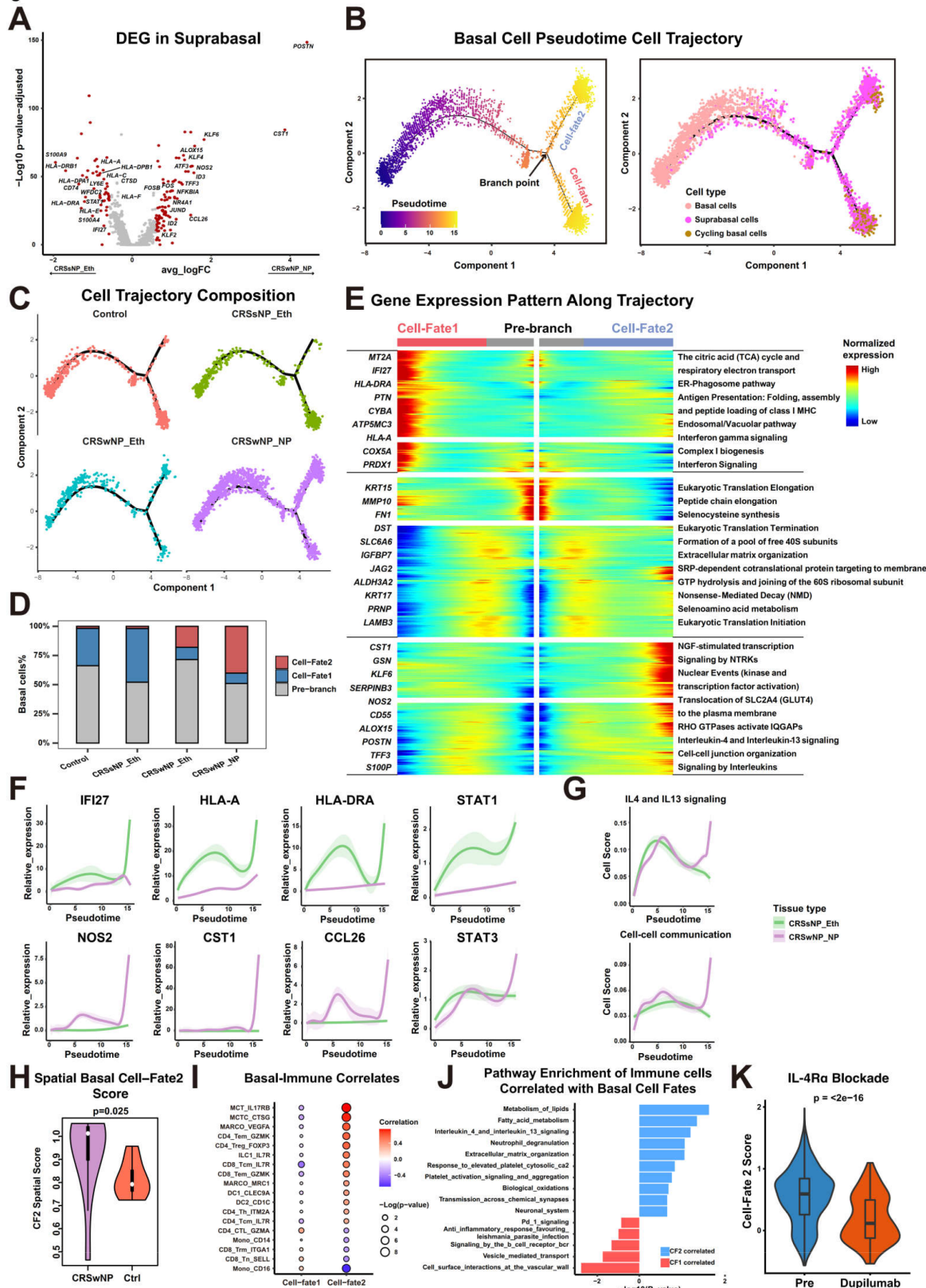


**Figure 6:** Nascent Basal Cells in Nasal Polyps Exhibit a Unique Transition Trajectory and Induce T2 Immune Response. (A) Volcano plot depicting differentially expressed genes in suprabasal cells between CRS nasal polyps and CRS without nasal polyps. The most significant genes are highlighted in red ( $|Foldchange| > 1.5$ ). (B) Pseudotime trajectory analysis for basal cells using Monocle (left panel), accompanied by a cell density plot of the three basal cell subtypes along the pseudotime axis (right panel). (C) Cell density plot illustrating the distribution of basal cells from CRS and control samples along the pseudotime trajectory. (D) Histogram displaying the distribution of basal cells from CRS and control samples in three phases identified in (B).

**Figure 6 continued:** (E) Gene expression dynamics along the basal cell trajectory outlined in (B), from the pre-branch phase to cell fate 1 and cell fate 2. Genes are clustered into three gene sets, each characterized by specific expression profiles, as demonstrated by marker genes (left) and enriched pathways (right) unique to each cluster. (F) Dynamic expression of genes upregulated in CRS nasal polyps (top panels) and CRS without nasal polyps (bottom panels) during basal cell transition along pseudotime in CRS nasal polyps (purple) and CRS without nasal polyps (green). (G) Dynamic expression score of functional pathway signatures upregulated in CRS nasal polyps during basal cell transition along pseudotime in CRS nasal polyps (purple) and CRS without nasal polyps (green). (H) Violin plots comparing expression scores of Cell-fate2 basal cell signature between CRS nasal polyps (purple) and healthy control samples (red) in DSP data within PanCK+ regions. (I) Dotplot illustrating the correlation between different cell-fate basal cells and immune cells. Correlations with a p-value < 0.2 are displayed. (J) Pathways enriched in the top 5 cells correlated with Cell-fate1/2 basal cells, based on GSEA analysis using the REACTOME gene set. (K) Violin plots comparing the expression scores of Cell-fate2 basal cell signature between basal cells in pre-treatment (blue) and post-treatment (red) nasal polyps samples from an individual treated with IL-4R $\alpha$  antibody.

429 cations for the development of immunomodulatory therapies 478  
430 targeting specific T cell subsets. 479

431 Another revealing finding was the enrichment of MCs within 480  
432 nasal polyp tissues, which strongly correlate with type II 481  
433 immune responses. We demonstrated that IL4/IL13-related 482  
434 ligand-receptor interactions between MCs and CD4+ T cells 483  
435 played a critical role in promoting Type II immunity in CR- 484  
436 SwNP. This finding underlines the dance between innate MCs 485  
437 in mediating acquired T cell immune responses observed in 486  
438 chronic upper airway inflammation, and suggests that target- 487  
439 ing MCs or their interactions with CD4+ T cells also repre- 488  
440 sent a promising therapeutic strategy for possibly modulating 489  
441 type II immune responses in CRSwNP. 490

442 Our analysis further suggested a critical correlation between 490  
443 Tuft epithelial cells and Th2 lymphoid cells in nasal poly- 491  
444 posis. Tuft cells were found to be involved in prostaglandin 492  
445 synthesis and regulation, with ALOX5 and PTGS1 expres- 493  
446 sion mediating interactions between Tuft cells and CD4+ 494  
447 T cells that expressed the PTGDR2 receptor in CRSwNP. 495  
448 This immune-epithelial interaction suggests that targeting 496  
449 Tuft cells or their mediators could represent an novel avenue 497  
450 for blunting and/or modulating Th2 cell-driven inflammation 498  
451 in CRSwNP. 499

452 Finally, we demonstrated that nascent basal cells in nasal 500  
453 polyps exhibited a unique transitional trajectory that may 501  
454 induce Type II immune responses. The distinct Cell-fate2 502  
455 basal cell trajectory identified within CRSwNP may provide 503  
456 a roadmap as to the aberrant epithelial regeneration observed 504  
457 in the mucosal tissues of these patients, with potential impli- 505  
458 cations for understanding the tissue remodeling and immune- 506  
459 trafficking processes observed in CRSwNP, including that of 507  
460 NP generation. Experimental validation using IL4 and IL13 508  
461 stimulation, or from dupilumab biologic treatment of a CR- 509  
462 SwNP patient, further underscored the potential for target- 510  
463 ing basal cell dynamics and the discrete interactions between 511  
464 epithelial progenitor cells and immunocyte populations as a 512  
465 novel treatment avenue. 513

466 These findings together serve to provide key insights into the 514  
467 epithelial-immune interactions within the tissue microenvi- 515  
468 ronment of CRS, and their roles in tissue remodeling, im- 516  
469 mune cell attraction, and ultimately, NP formation in CR- 517  
470 SwNP patients. By dissecting the subtle autocrine and 518  
471 paracrine cellular and molecular signaling interplay in CRS 519  
472 using higher-resolution tools, these multi-dimensional anal- 520  
473 yses implicate an array of pivotal actors and promising ther- 521  
474 apeutic targets for the modulation of both upper airway in- 522  
475 flammation and tissue remodeling processes in chronic rhi- 523  
476 nosinusitis. Further research is needed to validate these find- 524  
477 ings in larger cohorts, and to explore the true therapeutic po- 525

478 tential of decoupling immune-epithelial interactions in CRS. 479  
480 The multi-scaled transcriptomic resources generated herein 481  
482 will likely impact these future endeavors, and beyond. 483

## Materials & Methods

**Patient recruitment.** Patients were diagnosed with CR-SwNP and CRSsNP based on a European position paper on rhinosinusitis and nasal polyps (EPOS) 2012 and International Consensus of Allergy and Rhinology: Rhinosinusitis (ICAR:RS) guidelines. CRSwNP, CRSsNP, and controls were all recruited from Stanford University. Tissues from the ethmoid sinus mucosa or nasal polyps were collected during endoscopic sinus surgery. Five control patients underwent skull base surgery requiring ethmoid sinus surgery for treatment of cerebrospinal fluid leak, meningioma, or pituitary adenoma. None of the control patients had evidence of CRS or other upper airway inflammatory diseases on CT/MRI radiography or endoscopy. Patients with unilateral sinus disease, fungal or allergic fungal rhinosinusitis, antrochoanal polyps, cystic fibrosis, aspirin-exacerbated respiratory disease, or paranasal sinus cysts were excluded from this study. Patient characteristics, including demographics, medical history, and past medication use were collected. Patient data, including medication history, were independently verified through direct interview by a trained research technician/physician and by a questionnaire additionally administered on the day of surgery to confirm accuracy of existing records derived from patients' electronic medical or pharmacy. In particular, to avoid confounders in the epithelial/immune cell findings associated with use of common anti-inflammatory medications in CRS, all included CRSsNP and CRSwNP patients were devoid of oral prednisone/methyl-prednisolone exposure and higher dose topical budesonide and mometasone nasal irrigations x 4 weeks, as well as lower-dose topical nasal steroid sprays such as fluticasone and mometasone for 2 weeks, prior to ethmoid or NP tissue sampling. Antibiotic use within 4 weeks of surgery also led to exclusion. Any doubt in patient medication use led to exclusion from final analysis. Patients' characteristics are shown in Table 1. The study complied with the Declaration of Helsinki and all relevant ethical regulations of each institution, and written informed consent was obtained from each patient approved Institutional Review Board (IRB) protocols in accordance with the regulations of the Research Compliance Office at Stanford University (IRB 18981).

**Single-cell RNA sequencing and data processing.** Each sample was received directly from surgeons and promptly delivered to the laboratory on ice. Upon arrival at the labora-

tory, the samples were immediately processed. The ethmoid sinus mucosa was removed from the bone and nasal polyps were left intact and were minced into small pieces by scis-sors on ice. The minced tissues were placed into a C tube (Miltenyi Biotec, Bergisch Gladbach, Germany) within a solution of RPMI 1640 (Gibco, Grand Island, NY) containing 10% fetal bovine serum (FBS), 0.02 mg/ml DNase I (Millipore Sigma, St. Louis, MO), and 4 mg/ml collagenase type IV (Thermo Fisher Scientific). The mixture was homogenized using the gentleMACS Dissociator (Miltenyi Biotec) and incubated at 37°C for total of 30 minutes (15 minutes, 2 times) with rotated using MACSmix Tube Rotator (Miltenyi Biotec). Between and after the two incubations, they were also homogenized in a gentleMACS Dissociator. Finally, the samples were filtered through a 70-μm cell strainer and spun down at 500g for 5 min. Red blood cells (RBC) were lysed using the RBC Lysis Solution (BioLegend, San Diego, CA) for 4 min at room temperature. Cells were then washed with ice-cold PBS and spun down at 500g for 5 min at 4°C before resuspension in RPMI containing 10

The single cell suspension was loaded onto the Chromium Controller (10x Genomics) using the Chromium single cell 3' Reagent Kit v3 (10X Genomics), and scRNA-seq libraries generated in accordance with the manufacturer's protocols. Sequencing was performed on a Illumina HiSeq 4000 with 75 bp pair end reads.

The CellRanger v3.1.0 (10X Genomics) analysis pipeline was used to generate a final digital expression matrix. Raw sequence reads were preprocessed and mapped onto the reference human genome (GRCh38-3.0.0). These data were used as input into the Seurat package (4.1.1) (<https://github.com/satijalab/seurat>) for further analyses in R (4.2.0). As part of the quality control metrics, genes detected (UMI count > 0) in less than three cells, and cells containing a small number of genes detected (UMI count < 200) or high mitochondrial genome transcript ratio (25%) were removed. After normalizing and identifying variable features for each sample independently, the data from all the patients were combined using the top 30 dimensions in 'FindIntegrationAnchors()' and 'IntegrateData()' functions.

**Unsupervised clustering and cell type identification.** The normalized expression level was calculated for each gene by dividing the read counts for each cell by the total counts and multiplied by a scale factor of 1,000,000. The natural-log transformed values were taken as the final measurement of expression level for each gene in a specific cell. Based on the normalized expression level, we next selected a subset of genes that with high cell-to-cell variation in the dataset. Then, the principal component analysis (PCA) was performed on these variable genes. Following the results of PCA, Harmony was performed to correct the batch effect among samples (25), then an adequate number (30-40) determined by Elbowplot of principal components (PCs) were selected for dimensionality reduction and clustering. The UMap algorithm with a resolution parameter in a range of 0.1-0.8 was applied for dimensionality reduction and visualization (26). To identify marker genes that define a cluster,

differential expression analysis was performed by comparing each single cluster to all other cells. To accelerate the computational time of differential expression analysis, genes with > 0.25 log-fold difference on average between the two groups of cells and detectable in more than 25% of cells in either of the two groups of cells were retained. Using the above differentially expressed genes, cells were annotated to different cell types according to their well-known canonical markers. All the above analysis was performed using the Seurat R package (v 4.1.1)(27)

**Differentially expressed genes analysis in scRNA-seq data.** To define genes that may function in between CRS with and without nasal polyps, differential expression analysis in specific cell groups was performed using the 'FindMarkers' function implemented in the Seurat package. The Wilcoxon rank sum test with log-scaled fold change > 0.25 and adjusted P value < 0.05 (bonferroni correction) was performed to select differentially expressed genes.

**Pathway analysis.** To reveal the potential biological functions of T cells in two types of CRS, GSEA was performed with R package 'clusterProfiler' and 'ReactomePA' to identify pathway enriched under the REACTOME gene sets released by MsigDB (28-31). In Tuft cells, differentially expressed genes identified between CRS with and without nasal polyps were used to perform WikiPathway enrichment (32). Pathways that have a BH-adjusted P value () smaller than 0.05 were defined as being significantly enriched, and GSEA was performed to further validate the pathway enrichment.

**Definition and calculation of gene signature scores.** To assess the functional status of specific cells, relative signatures were collected from published literature as follows. A M2 signature was used to define the functional phenotype of macrophages. An inflammatory signature (32), Th1 and Th2 signature (33, 34) were used to assess T cell functions. In scRNA data, expression scores of specific signatures were calculated using AddModuleScore in the Seurat package. To validate the interaction between basal cells and T2 immune response, the expression score and enrichment of cell fate signatures were accessed in public single cell and bulk RNA-seq datasets (10). All genes associated with each pathway score are available in Supp Table 2. Violinplot was adopted to present the scoring difference among different types of CRS and healthy control samples, and Wilcoxon rank-sum test was performed to indicate the statistical significance.

**Construction of cell developmental trajectory.** The developmental trajectory of the basal cells was inferred using the Monocle2 package (10). The 10x Genomics sequencing data was first imported into Monocle2 in CellDataSet class, and the negative binomial distribution was chosen to model the reads count data. Differentially expressed genes across different cell populations were identified and selected as input features to construct the trajectory. Then, a Reversed Graph Embedding algorithm was performed to reduce the data's dimensionality. With the expression data projected into

636 a lower dimensional space, cells were ordered in pseudotime 692  
637 and trajectory was built to describe how cells transit from 693  
638 one state into another. After the cell trajectories were con- 694  
639 structed, differentially expressed genes along the pseudotime 695  
640 trajectory separated by the branch point were detected using 696  
641 the 'differentialGeneTest' function. For each interested gene, 697  
642 the expression trend along the pseudotime was estimated us- 698  
643 ing non-linear regression, and plotted with a curve chart.

644 **Inference of cell-cell communications.** R package 699  
645 Cellchat (v1.5.0) was adopted to identify significant ligand- 700  
646 receptor pairs within different types of CRS samples (35). 701  
647 Ligand-receptor communication probabilities/strengths were 702  
648 computed, tested, compared and visualized on the samples 703  
649 of CRS with and without nasal polyps. The minimum 704  
650 communication cells threshold was set to 10 and other 705  
651 parameters were left as default.

652 **GeoMx-Digital Spatial Profiling.** Samples collected for 708  
653 NanoString GeoMx-Digital Spatial Profiling were fixed in 10 709  
654 Slides were deparaffinized and prepared according to the of- 710  
655 ficial NanoString GeoMx-NGS RNA Manual Slide Prepara- 711  
656 tion protocol (36). In brief, slides were baked for 30 min at 712  
657 60°C before washing in Xylene (3 x washes at 5 min each), 713  
658 100% EtOH (2 x washes at 5 min each), 95% EtOH (1 x wash 714  
659 at 5 min) and in 1X PBS (1 x wash at 1 min). Slides then un- 715  
660 derwent heat induced epitope retrieval at 99°C for 10 min in 716  
661 Tris-EDTA retrieval buffer (eBioscience, 00-4956-58). 717  
662 Slides were then digested by Protease K (0.1µg/ml) for 5 718  
663 mins at 37°C, and then washed with 1X PBS. Subsequently, 719  
664 slides were fixed by 10% neutral buffered formalin (EMS Di- 720  
665 asum, 15740-04) for 5 min at room temperature, then the 721  
666 fixation process was stopped by 5 mins of 1X NBF Stop 722  
667 Buffer wash, followed by 5 mins of 1X PBS wash. The 723  
668 NanoString DSP Human CTA detection probe cocktail was 724  
669 then applied to the slides and incubated overnight ( 18 hrs) 725  
670 at 37°C. After hybridization, slides were washed in Strin- 726  
671 gent Wash Buffer (2X SSC, 50% Formamide) 2 times, ev- 727  
672 ery 5 mins. Slides were then washed by 2X SSC twice, 2 728  
673 mins each. Buffer W was then applied to the slides for 30 729  
674 mins, followed by antibody staining for 1hrCD45 D9M8I, 730  
675 Cell Signaling Technologies), PanCK (AE1+AE3, Novus). 731  
676 Slides were then washed by 2X SSC twice, 5mins each, and 732  
677 stained with 500nM SYTO 13 for 15 min, then loaded on 733  
678 the GeoMx machine. For GeoMx DSP sample collection, 734  
679 we followed the instructions described in the GeoMx DSP 735  
680 instrument user manual (MAN-10088-03). Briefly, individ- 736  
681 ual ROIs were then selected the areas immune cells aggre- 737  
682 gate and epithelium presented on the apical side of the tis- 738  
683 sues which includes ROI based on CD45 positive or PanCK 739  
684 positive masks were selected with the consent of two or more 740  
685 investigators. On average, the ROI sizes are approximately 741  
686 45217 um<sup>2</sup> for CD45+ regions and 37501 um<sup>2</sup> for PanCK+ 743  
687 regions. After sample collection, the NanoString NGS library 744  
688 preparation kit was used: Each ROI was uniquely indexed us- 745  
689 ing Illumina's i5 x i7 dual-indexing system. In total, 4 µL of 746  
690 collected sample was used in a PCR reaction with 1 µM of i5 747  
691 primer, 1 µM i7 primer, and 1 x NanoString library prep PCR 749

Master Mix. PCR reaction conditions were 37°C for 30 min, 50 °C for 10 min, 95°C for 3 min, 18 cycles of 95°C for 15 s, 65 °C for 60 s, 68°C for 30s, and final extension of 68°C for 5min. Then the product was purified with two rounds of AMPure XP beads (Beckman Coulter) at 1.2 x bead-to-sample ratio. Libraries were paired-end sequenced (2 × 75) on a NextSeq550.

**Digital Spatial Profiling Data Analysis.** Probes from the NanoString CTA panel were mapped and counted using the NanoString GeoMx Data Analysis software pipeline (36), using the FASTQ output from NGS sequencing. Thereafter, the data underwent quality control and normalization steps with the 'Geomx-Tools' software from NanoString: First, ROI and probes that did not meet the default QC requirement were filtered out and not used in the subsequent analysis. Next, raw probe counts were transferred into a gene-level count matrix by calculating the geometric mean of probes for each gene. Normalization of gene counts were then performed, with the 'Q3 norm' method in 'Geomx-Tools'. The Q3 normed gene counts were then used for all subsequent downstream analysis.

Mean levels of spatial region-specific gene expression or mean levels of spatial expression scores of specific signatures, and also their correlations were adopted to validate corresponding results or hypotheses. Apart from published signatures, differential expressed genes identified in scRNA data were also applied to validate cell phenotype and function in the DSP data, and spatial region-specific expression scores were calculated with ssGSEA using the GSVA package (37). The Wilcoxon rank sum test was performed to calculate the significance of differences between samples.

**Statistical Analysis.** All data analyses were conducted in R 4.2.0. Statistical significance was defined as a two-sided P value of less than 0.05. The comparison of cell fractions, expression levels of marker genes and gene signature scores among different types of CRS and control samples were performed using Wilcoxon rank sum test. The correlation analyses were performed using Spearman's correlation test.

#### ACKNOWLEDGEMENTS

The authors thank members of the Jiang and Nayak laboratories for insightful discussions. S.J. is supported by NIH DP2AI171139, R01AI149672, a Gilead's Research Scholars Program in Hematologic Malignancies, and the Bill & Melinda Gates Foundation INV-002704. J.V.N. is supported by R01HL151677, 1U54CA260517, and U19 AI171421. This article reflects the views of the authors and should not be construed as representing the views or policies of the institutions that provided funding.

S.J. has received speaking honorariums from Cell Signaling Technology unrelated to this work. G.P.N., is co-founder of IonPath Inc and Akoya Biosciences, Inc., inventor on patent US9909167, and is a Scientific Advisory Board member for Akoya Biosciences, Inc. The other authors declare no competing interests.

#### AUTHOR CONTRIBUTIONS

Conceptualization: S.J., I.T.L., T.N., J.V.N.

Methodology and Analysis: G.L., T.N., I.T.L., B.Z., J.V.N., S.J.

Novel Reagents and Tools: D.T.B., C.H.Y., J.B.O., D.Z., S.S.D., P.A.G., A.Y., D.K., K.P., M.T.C., M.L., Z.M.P., P.H.H., D.W., J.C., Q.M., Z.L., G.P.N., D.B.

Writing – Original Draft: S.J., J.V.N., G.L., I.T.L., T.N., B.Z.

Writing – Reviewing and Editing: all authors

Supervision: S.J., J.V.N.

## 750 References

751 1. Adam S DeConde and Zachary M Soler. Chronic rhinosinusitis: epidemiology and burden 837  
752 of disease. *American journal of rhinology & allergy*, 30(2):134–139, 2016. 838

753 2. Dirk Dietz de Loos, Evelijn S Lourijen, Maarten AM Wilderman, Nicole JM Freling, Marije DJ 839  
754 Wolvers, Sietze Reitsma, and Wytseke J Fokkens. Prevalence of chronic rhinosinusitis in the 840  
755 general population based on sinus radiology and symptomatology. *Journal of Allergy and 841  
756 Clinical Immunology*, 143(3):1207–1214, 2019. 842

757 3. Mariel R Benjamin, Whitney W Stevens, Newton Li, Sumit Bose, Leslie C Grammer, 843  
758 Robert C Kern, Bruce K Tan, David B Conley, Stephanie S Smith, Kevin C Welch, et al. 844  
759 Clinical characteristics of patients with chronic rhinosinusitis without nasal polyps in an aca- 845  
760 demic setting. *The Journal of Allergy and Clinical Immunology: In Practice*, 7(3):1010–1016, 846  
761 2019. 847

762 4. Claus Bachert, Bradley Marple, Rodney J Schlosser, Claire Hopkins, Robert P Schleimer, 848  
763 Bart N Lambrecht, Barbara M Bröker, Tanya Laidlaw, and Woo-Jung Song. Adult chronic 849  
764 rhinosinusitis. *Nature Reviews Disease Primers*, 6(1):86, 2020. 850

765 5. Daniel Rosenblum and Shruti Naik. Epithelial–immune crosstalk in health and disease, 851  
766 *Current Opinion in Genetics & Development*, 74:10190–10190, 2022. 852

767 6. Laure Guenin-Mace, Piotr Konieczny, and Shruti Naik. Immune-epithelial cross talk in re- 853  
768 generation and repair. *Annual Review of Immunology*, 41:207–228, 2023. 854

769 7. Atsushi Kato, Anju T Peters, Whitney W Stevens, Robert P Schleimer, Bruce K Tan, and 855  
770 Robert C Kern. Endotypes of chronic rhinosinusitis: relationships to disease phenotypes, 856  
771 pathogenesis, clinical findings, and treatment approaches. *Allergy*, 77(3):812–826, 2022. 857

772 8. Masami Taniguchi, Enrico Heffler, Heidi Olze, Andrew White, Joana Corte-Real, Petter Ols- 858  
773 son, and Slawomir Lazarewicz. The role of omalizumab in nsaid-exacerbated respiratory 859  
774 disease: a narrative review. *The Journal of Allergy and Clinical Immunology: In Practice*, 860  
775 2022. 861

776 9. Tetsuji Takabayashi and Robert P Schleimer. Formation of nasal polyps: the roles of innate 862  
777 type 2 inflammation and deposition of fibrin. *Journal of Allergy and Clinical Immunology*, 863  
778 145(3):740–750, 2020. 864

779 10. Jose Ordovas-Montanes, Daniel F Dwyer, Sarah K Nyquist, Kathleen M Buchheit, Marko 865  
780 Vukovic, Chaarushena Deb, Marc H Wadsworth, Travis K Hughes, Samuel W Kazer, Eri 866  
781 Yoshimoto, et al. Allergic inflammatory memory in human respiratory epithelial progenitor 867  
782 cells. *Nature*, 560(7720):649–654, 2018. 868

783 11. Robert P Schleimer. Immunopathogenesis of chronic rhinosinusitis and nasal polypsis. 869  
784 *Annual Review of Pathology: Mechanisms of Disease*, 12:331–357, 2017. 870

785 12. Dawn T Bravo, Ethan Soudry, Justin A Edward, Wei Le, Alan L Nguyen, Peter H Hwang, 871  
786 Mrinmoy Sanyal, and Jayakar V Nayak. Characterization of human upper airway epithelial 872  
787 progenitors. In *International Forum of Allergy & Rhinology*, volume 3, pages 841–847. Wiley 873  
788 Online Library, 2013. 874

789 13. Jayakar V Nayak, Aakanksha Rathor, Jessica W Grayson, Dawn T Bravo, Nathalia Ve- 875  
790 lasquez, Julia Noel, Daniel M Beswick, Kristen O Riley, Zara M Patel, Do-Yeon Cho, et al. 876  
791 Porcine small intestine submucosal grafts improve remucosalization and progenitor cell re- 877  
792 cruitment to sites of upper airway tissue remodeling. In *International Forum of Allergy & 878  
793 Rhinology*, volume 8, pages 1162–1168. Wiley Online Library, 2018. 879

794 14. Tsuguhisa Nakayama, Ivan T Lee, Wei Le, Yasuhiro Tsunemi, Nicole A Borchard, David 880  
795 Zarabanda, Sachi S Dholakia, Philip A Gall, Angela Yang, Dayoung Kim, et al. Inflammatory 881  
796 molecular endotypes of nasal polyps derived from white and japanese populations. *Journal 882  
797 of Allergy and Clinical Immunology*, 149(4):1296–1308, 2022. 883

798 15. Lei Zhang, Ziyi Li, Katarzyna M Skrzypczynska, Qiao Fang, Wei Zhang, Sarah A O'Brien, 884  
799 Yao He, Lynn Wang, Qiming Zhang, Aeryon Kim, et al. Single-cell analyses inform mecha- 885  
800 nisms of myeloid-targeted therapies in colon cancer. *Cell*, 181(2):442–459, 2020. 886

801 16. Yunfan Sun, Liang Wu, Yu Zhong, Kaiqian Zhou, Yong Hou, Zifei Wang, Zefan Zhang, Jiarui 887  
802 Xie, Chunqing Wang, Dandan Chen, et al. Single-cell landscape of the ecosystem in early- 888  
803 relapse hepatocellular carcinoma. *Cell*, 184(2):404–421, 2021. 889

804 17. Mariagrazia Uggioni, Pius Loetscher, Ulf Forssmann, Beatrice Dewald, Haodong Li, 890  
805 S Hensche Lima, Yuling Li, Brent Kreider, Gianni Garotta, Marcus Thelen, et al. Mono- 891  
806 cyte chemotactic protein 4 (mcp-4), a novel structural and functional analogue of mcp-3 and 892  
807 eotaxin. *The Journal of experimental medicine*, 183(5):2379–2384, 1996. 893

808 18. Eduardo A Garcia-Zepeda, Christophe Combadiere, Marc E Rothenberg, Mindy N Sarafi, 894  
809 Frank Lavigne, Qutayba Hamid, Philip M Murphy, and Andrew D Luster. Human mono- 895  
810 cyte chemoattractant protein (mcp)-4 is a novel cc chemokine with activities on monocytes, 896  
811 eosinophils, and basophils induced in allergic and nonallergic inflammation that signals 897  
812 through the cc chemokine receptors (ccr)-2 and -3. *Journal of immunology (Baltimore, Md.: 898  
813 1950)*, 157(12):5613–5626, 1996. 899

814 19. Elena Denisenko, Belinda B Guo, Matthew Jones, Rui Hou, Leanne De Kock, Timo Lass- 900  
815 mann, Daniel Poppe, Olivier Clément, Rebecca K Simmons, Ryan Lister, et al. Systematic 901  
816 assessment of tissue dissociation and storage biases in single-cell and single-nucleus rna- 902  
817 seq workflows. *Genome biology*, 21(1):1–25, 2020. 903

818 20. Murugappan Ramanathan Jr, Won-Kyung Lee, Ernst W Spannake, and Andrew P Lane. 904  
819 Th2 cytokines associated with chronic rhinosinusitis with polyps down-regulate the antimicro- 905  
820 bial immune function of human sinonasal epithelial cells. *American journal of rhinology*, 906  
821 22(2):115–121, 2008. 907

822 21. Atsushi Kato. Immunopathology of chronic rhinosinusitis. *Allergology International*, 64(2): 908  
823 121–130, 2015. 909

824 22. Daniel F Dwyer, Jose Ordovas-Montanes, Samuel J Allon, Kathleen M Buchheit, Marko 910  
825 Vukovic, Tahereh Derakhshan, Chunli Feng, Juying Lai, Travis K Hughes, Sarah K Nyquist, 911  
826 et al. Human airway mast cells proliferate and acquire distinct inflammation-driven phenotypes 912  
827 during type 2 inflammation. *Science immunology*, 6(56):eabb7221, 2021. 913

828 23. Claus Bachert, Leda Mannent, Robert M Naclerio, Joaquin Mullol, Berrylin J Ferguson, 914  
829 Philippe Gevaert, Peter Hellings, Lixia Jiao, Lin Wang, Robert R Evans, et al. Effect of 915  
830 subcutaneous dupilumab on nasal polyp burden in patients with chronic sinusitis and nasal 916  
831 polypsis: a randomized clinical trial. *Jama*, 315(5):469–479, 2016. 917

832 24. Claus Bachert, Joseph K Han, Martin Desrosiers, Peter W Hellings, Nikhil Amin, Stella E 918  
833 Lee, Joaquim Mullol, Leon S Greos, John V Bosso, Tanya M Laidlaw, et al. Efficacy and 919  
834 safety of dupilumab in patients with severe chronic rhinosinusitis with nasal polyps (liberty 920  
835 np sinus-24 and liberty np sinus-52): results from two multicentre, randomised, double-blind, 921  
836 placebo-controlled, parallel-group phase 3 trials. *The Lancet*, 394(10209):1638–1650, 922  
837 2019. 923

838 25. Ilya Korsunsky, Nghia Millard, Jean Fan, Kamil Slowikowski, Fan Zhang, Kevin Wei, Yuriy 924  
839 Baglaenko, Michael Brenner, Po-ru Loh, and Soumya Raychaudhuri. Fast, sensitive and 925  
840 accurate integration of single-cell data with harmony. *Nature methods*, 16(12):1289–1296, 926  
841 2019. 927

842 26. Etienne Becht, Leland McInnes, John Healy, Charles-Antoine Dutertre, Immanuel WH 928  
843 Kwok, Lai Guan Ng, Florent Giroux, and Evan W Newell. Dimensionality reduction for 929  
844 visualizing single-cell data using umap. *Nature biotechnology*, 37(1):38–44, 2019. 930

845 27. Yuhan Hao, Stephanie Hao, Erica Andersen-Nissen, William M Mauck, Shiwei Zheng, 931  
846 Andrew Butler, Maddie J Lee, Aaron J Wilk, Charlotte Darby, Michael Zager, et al. Integrated 932  
847 analysis of multimodal single-cell data. *Cell*, 184(13):3573–3587, 2021. 933

848 28. Tianzhi Wu, Erqiang Hu, Shuangbin Xu, Meijun Chen, Pingfan Guo, Zehan Dai, Tingze 934  
849 Feng, Lang Zhou, Wenli Tang, Li Zhan, et al. clusterprofiler 4.0: A universal enrichment 935  
850 tool for interpreting omics data. *The Innovation*, 2(3):100141, 2021. 936

851 29. Guangchuang Yu and Qing-Yu He. Reactomepa: an r/bioconductor package for reactome 937  
852 pathway analysis and visualization. *Molecular BioSystems*, 12(2):477–479, 2016. 938

853 30. Arthur Liberzon, Aravind Subramanian, Reid Pinchback, Helga Thorvaldsdottir, Pablo 939  
854 Tamayo, and Jill P Mesirov. Molecular signatures database (msigdb) 3.0. *Bioinformatics*, 27 940  
855 (12):1739–1740, 2011. 941

856 31. Marc Gillespie, Bijay Jassal, Ralf Stephan, Marija Milacic, Karen Rothfels, Andrea Senff- 942  
857 Ribeiro, Johannes Griss, Cristoffer Sevilla, Lisa Matthews, Chuqiao Gong, et al. The reactome 943  
858 pathway knowledgebase 2022. *Nucleic acids research*, 50(D1):D687–D692, 2022. 944

859 32. Marvin Martens, Ammar Ammar, Anders Riutta, Andra Waagmeester, Denise N Sleter, 945  
860 Kristina Hanspers, Ryan A. Miller, Daniela Digles, Elisson N Lopes, Friederike Ehrhart, 946  
861 et al. Wikipathways: connecting communities. *Nucleic acids research*, 49(D1):D613–D621, 947  
862 2021. 948

863 33. Mikel Ruterbusch, Kurt B Pruner, Laila Shehata, and Marion Pepper. In vivo cd4+ t cell 949  
864 differentiation and function: revisiting the th1/th2 paradigm. *Annual review of immunology*, 950  
865 38:705–725, 2020. 951

866 34. Rishi Vishal Luckheram, Rui Zhou, Asha Devi Verma, and Bing Xia. Cd4+ t cells: differen- 952  
867 tiation and functions. *Clinical and developmental immunology*, 2012, 2012. 953

868 35. Suoqin Jin, Christian F Guerrero-Juarez, Lihua Zhang, Ivan Chang, Raul Ramos, Chen- 954  
869 Hsiang Kuan, Peggy Myung, Maksim V Plikus, and Qing Nie. Inference and analysis of 955  
870 cell-cell communication using cellchat. *Nature communications*, 12(1):1088, 2021. 956

871 36. Christopher R Merritt, Giang T Ong, Sarah E Church, Kristi Barker, Patrick Danaher, Gary 957  
872 Geiss, Margaret Hoang, Jaemyeong Jung, Yan Liang, Jill McKay-Fleisch, et al. Multiplex 958  
873 digital spatial profiling of proteins and rna in fixed tissue. *Nature biotechnology*, 38(5):586– 959  
874 599, 2020. 960

875 37. Sonja Hänzelmann, Robert Castelo, and Justin Guinney. Gsva: gene set variation analysis 961  
876 for microarray and rna-seq data. *BMC bioinformatics*, 14:1–15, 2013. 962

877 **Supplementary Figures**

**Figure1S**

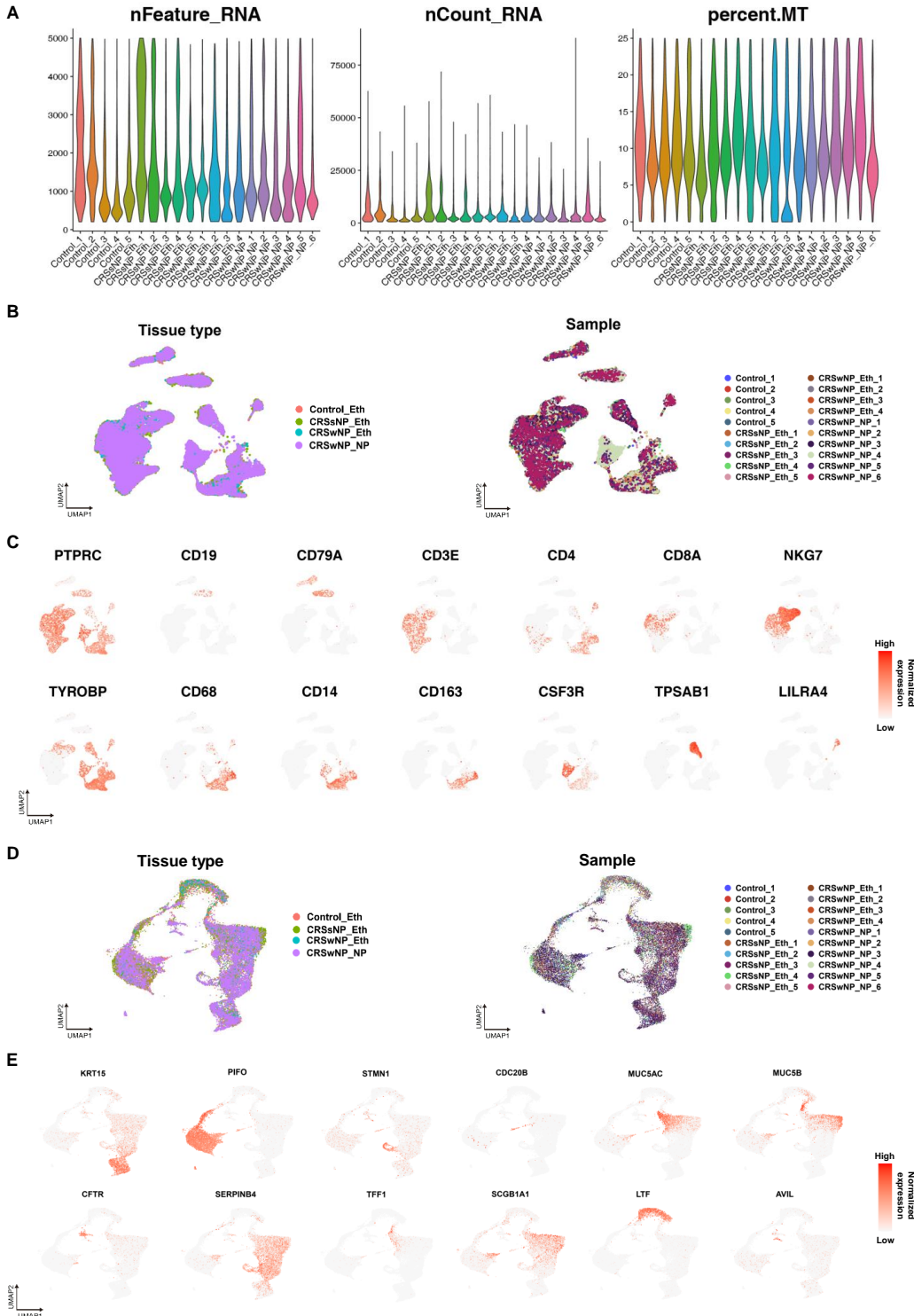


**Figure S1. Comprehensive Single-Cell Transcriptomic Analysis Reveals the Complex Immune and Epithelial Microenvironment in CRS, related to Figure1.** (A) Violin plots showing number of unique genes (left), number of total molecules (middle) and percentage of mitochondrial counts (right) of each cell in the single cell dataset. (B) UMAP plots showing immune cell origins by color, the origin of tissue types (left panel) and the origin of patient samples (right panel). (C) UMAP plot showing the expression of selected marker genes for the defined immune cell groups. (D) UMAP plots showing epithelial cell origins by color, the origin of tissue types (left panel) and the origin of patient samples (right panel). (E) UMAP plot showing the expression of selected marker genes for the defined epithelial cell groups.

**Figure2S**

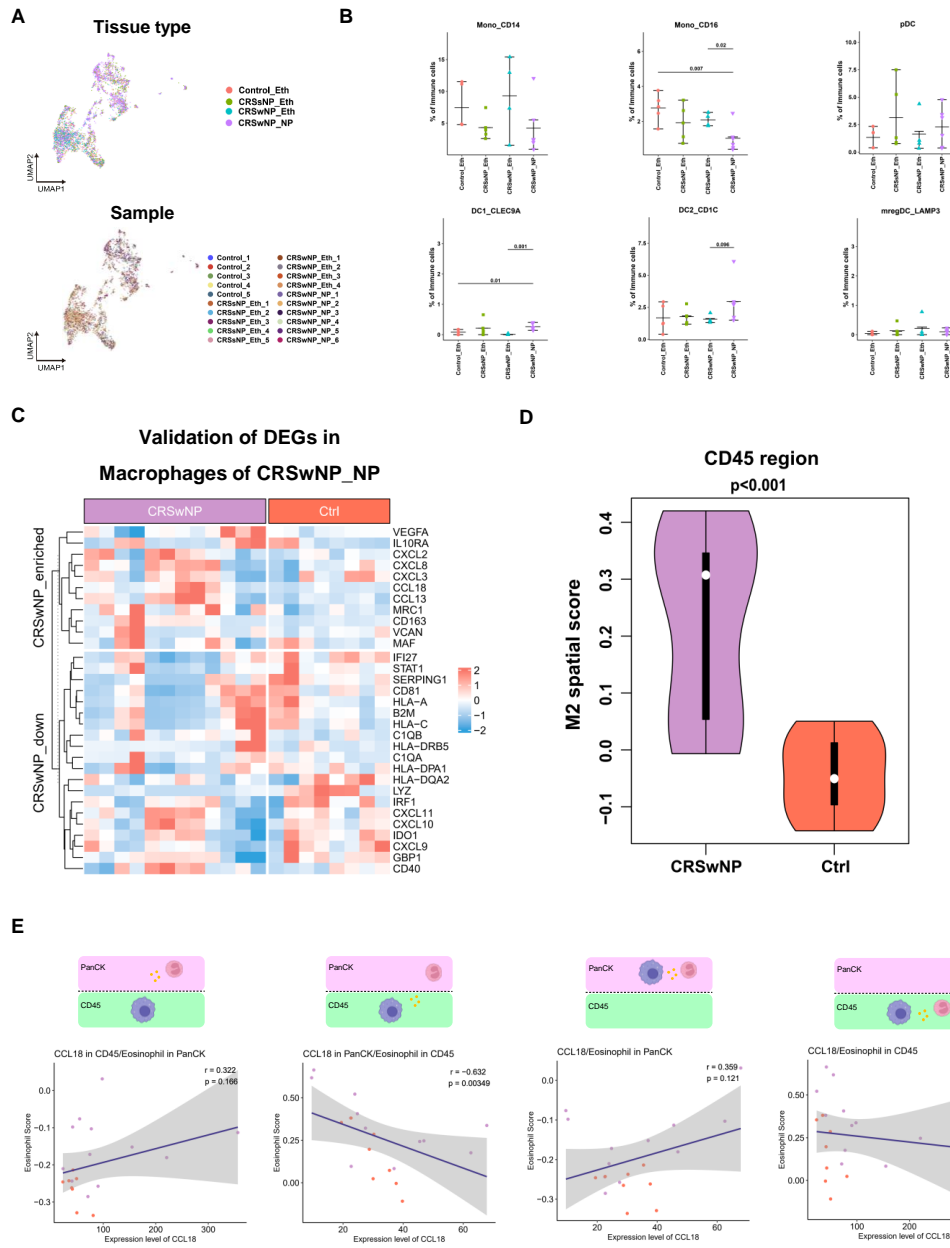


**Figure S2. Polarization of Macrophages to M2 Phenotype Drives Type 2 Inflammation in CRS Nasal Polyps, related to Figure2.** (A) UMAP plots showing myeloid cell origins by color, the origin of tissue types (upper panel) and the origin of patient samples (bottom panel). (B) Comparison of other myeloid cell fractions between CRS and control samples using the Wilcoxon test (two-sided). (C) Heatmap illustrating the normalized expression of genes upregulated and downregulated in nasal polyp macrophages in CD45+ regions of GeoMx data. (D) Violin plots comparing expression scores of M2 signature between CRS nasal polyps (purple) and healthy control samples (red) in GeoMx data within CD45+ regions. (E) Scatter plots illustrating the correlation between CCL18 expression levels and eosinophil signature scores in CD45+ or PanCK+ regions of GeoMx data, with sample origins color-coded to represent CRS nasal polyps (purple) and healthy control samples (orange). Diagrams above the scatter plots indicate regions where CCL18 and eosinophil spatial gene signatures were captured.

**Figure3S**

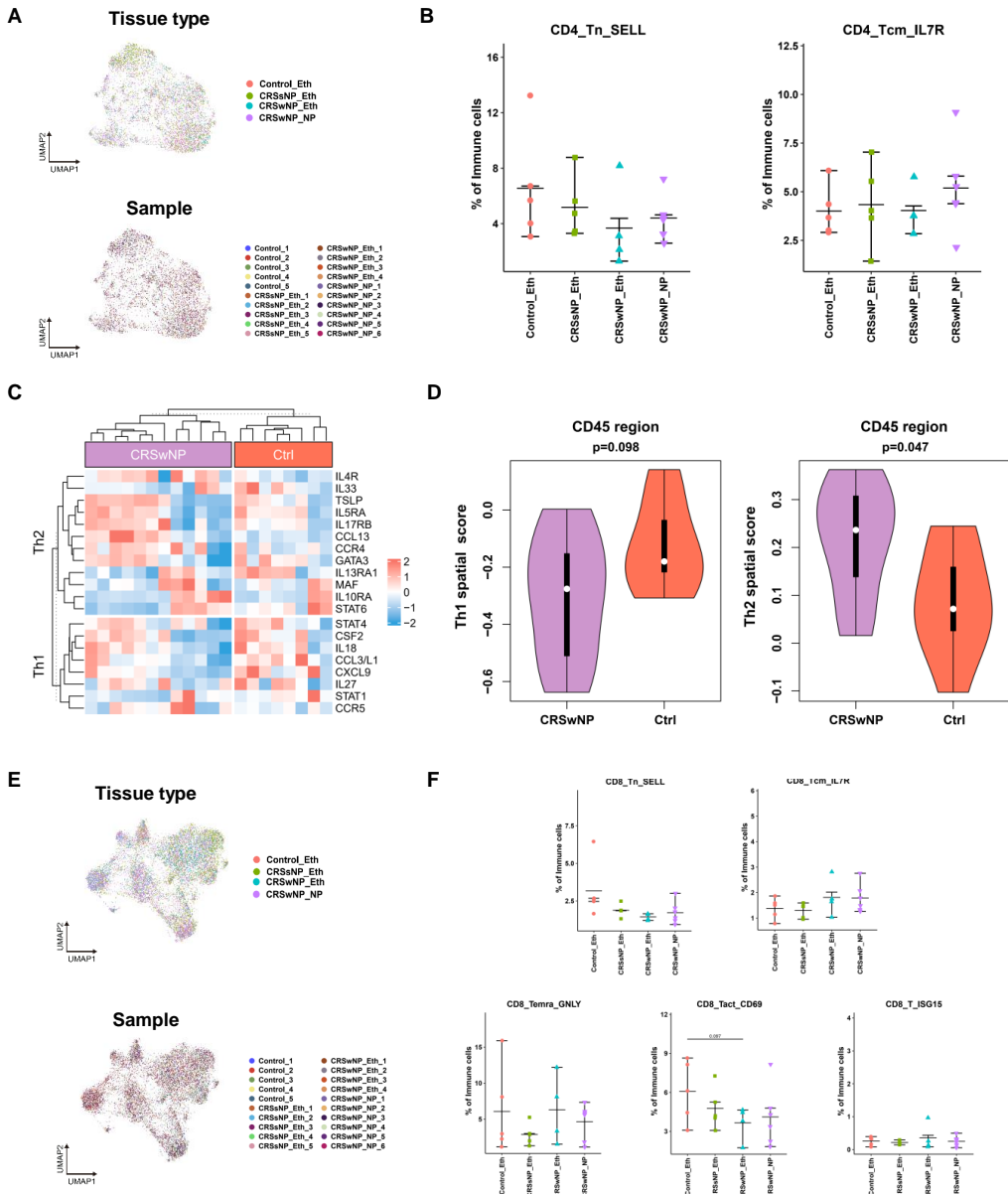


**Figure S3. Regulatory CD4+ and CD8+ T Cells Predominate in Nasal Polyps, related to Figure3.** (A) UMAP plots showing CD4+ T cell origins by color, the origin of tissue types (upper panel) and the origin of patient samples (bottom panel). (B) Comparison of other CD4+ T cell fractions between CRS and control samples using the Wilcoxon test (two-sided). (C) Heatmap illustrating the normalized expression of Th1/2 marker genes in CD45+ regions of GeoMx data. (D) Violin plots comparing expression scores of Th1/2 signatures between CRS nasal polyps (purple) and healthy control samples (red) in GeoMx data within CD45+ regions. (E) UMAP plots showing CD8+ T cell origins by color, the origin of tissue types (upper panel) and the origin of patient samples (bottom panel). (F) Comparison of other CD8+ T cell fractions between CRS and control samples using the Wilcoxon test (two-sided).

**Figure4S**

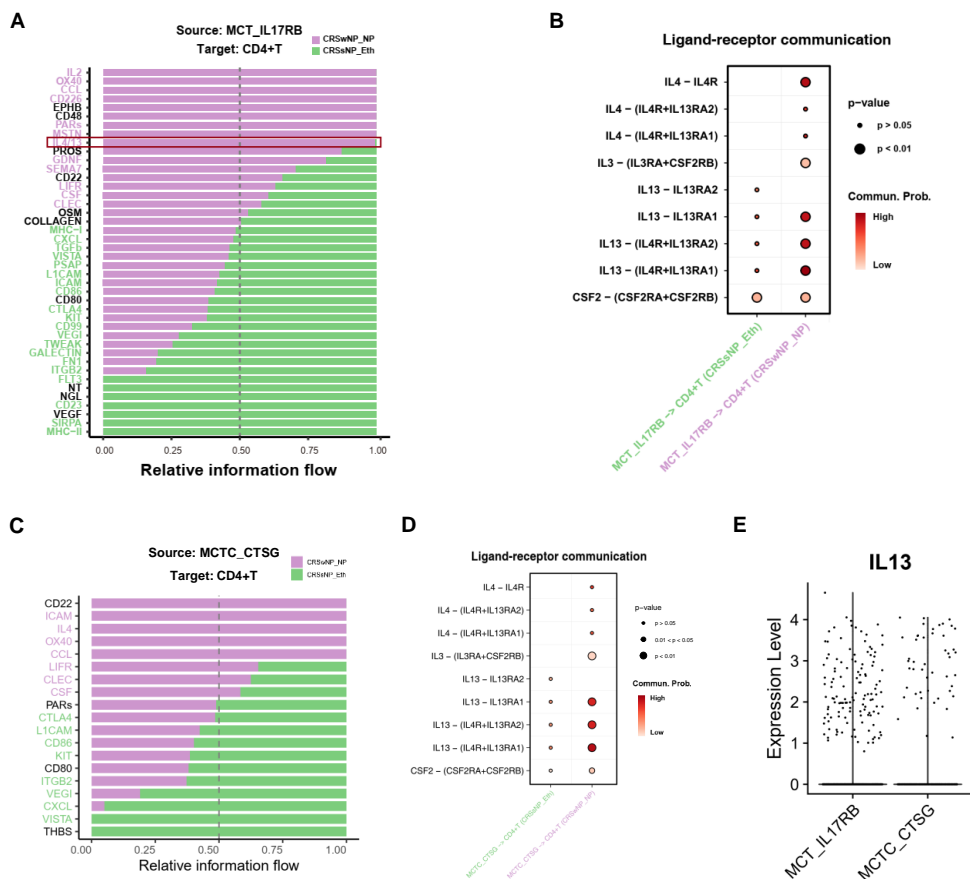


**Figure S4. Mast Cell Enrichment in Nasal Polyps Correlates with Type 2 Immune Responses, related to Figure4.** (A, C) Ligand-receptor (L-R) interactions identified between two subtypes of mast cells, MCT\_IL17RB(A)/MCTC\_CTSG(C) and CD4+ T cells in CRSwNP (purple) and CRSsNP (green). L-R pairs with purple bars crossing the 0.5 dotted line indicate predominance in CRSwNP, while those with green bars crossing the dotted line indicate predominance in CRSsNP. Significant interactions are color-coded accordingly ( $p < 0.05$ , Wilcoxon test). (B, D) Dot plot demonstrating the significance and strength of IL4/IL13-related ligand-receptor interactions between two subtypes of mast cells, MCTC\_CTSG(B)/MCTC\_CTSG(D) and CD4+ T cells in CRSwNP (purple) and CRSsNP (green). (E) Scatter plots depicting IL4 and IL13 expression levels in mast cell subtypes, and their enrichment in MCTC\_CTSG.

**Figure 5S**

**A**

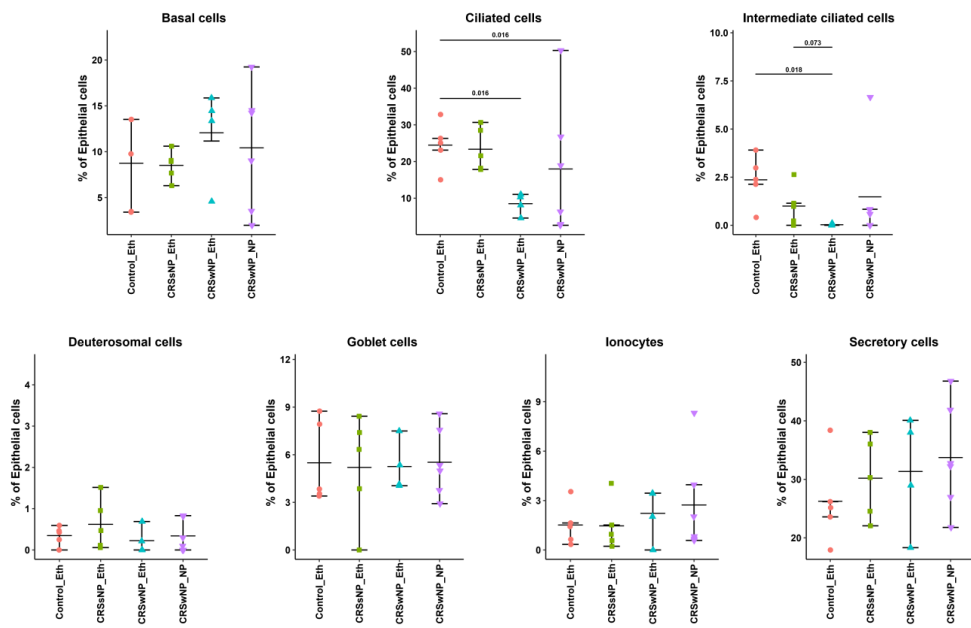


**Figure 5S. Epithelial composition difference in CRS, related to Figure 5.** Comparison of other epithelial cell fractions between CRS and control samples using the Wilcoxon test (two-sided).

**Figure6S**

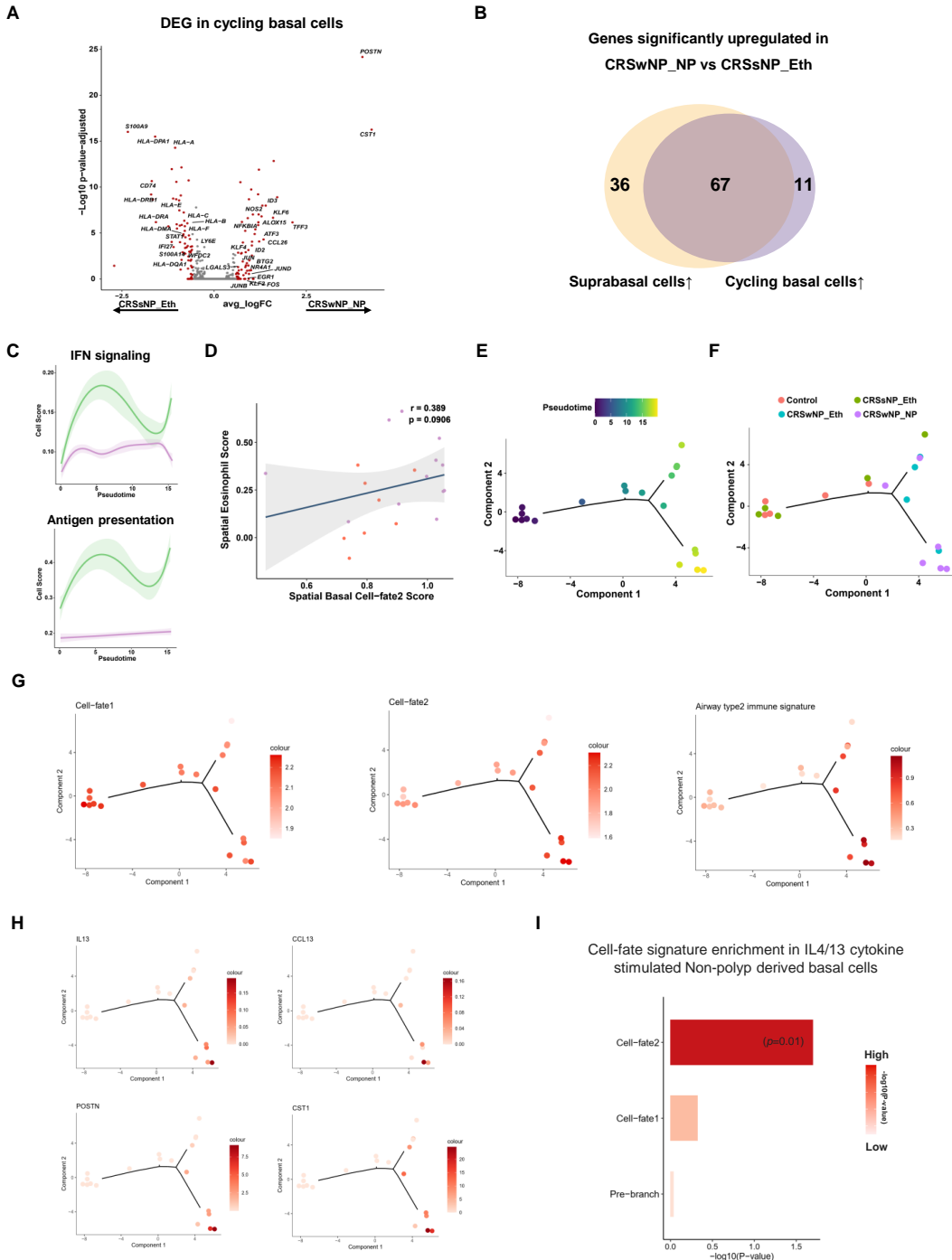


**Figure S6. Nascent Basal Cells in Nasal Polyps Exhibit a Unique Transition Trajectory and Induce T2 Immune Response, related to Figure6.** (A) Volcano plot depicting differentially expressed genes in cycling basal cells between CRS nasal polyps and CRS without nasal polyps. The most significant genes are highlighted in red ( $|Fold\ change| > 1.5$ ). (B) Venn plot depicting overlap between upregulated genes in suprabasal cells and cycling cells in nasal polyps. (C) Dynamic expression score of functional pathway signatures upregulated in CRS without nasal polyps during basal cell transition along pseudotime in CRS nasal polyps (purple) and CRS without nasal polyps (green). (D) Scatter plot and regression line illustrating the correlation between Cell-fate2 basal cell spatial gene signature expression scores in PanCK+ regions and eosinophil cell spatial gene signature expression scores in CD45+ regions. Dots are colored to represent patient sample origins. The grey region indicates the confidence interval. The regression index and p-values are shown in the plots. (E) Pseudotime trajectory analysis for pseudo-bulk data of each sample in the single cell dataset using differentially expressed genes among the three branches in Figure 6B for ordering. (F) Cell density plot illustrating the distribution of CRS and control samples along the pseudotime trajectory. (G) Pseudotime plot showing the expression of basal cell-fate signatures for pseudo-bulk samples along the trajectory. (H) Pseudotime plot showing the expression of genes upregulated in CRS nasal polyps during basal cell transition along the trajectory. (I) Barplot showing the enrichment of basal cell-fate signature in IL4/13 cytokine stimulated Non-polyp derived basal cells compared with Non-polyp derived basal cell baseline.